Analysis of multi-condition single-cell data with latent embedding multivariate regression

Constantin Ahlmann-Eltze[⋆,†] and Wolfgang Huber[⋆]

[⋆] *Genome Biology Unit, EMBL, Heidelberg, 69117, Germany.*
[†] *Collaboration for joint PhD degree between EMBL and Heidelberg University, Faculty of Biosciences*

27th of February 2024

Abstract

Identifying gene expression differences in heterogeneous tissues across experimental or observational conditions is a fundamental biological task, enabled by single-cell resolution assays such as multi-condition sc-RNA-seq. Current approaches divide the constituent cells into clusters meant to represent cell types, and identify differentially expressed genes for each cluster. However, such discrete categorization is often unsatisfactory: if too coarse, subtle but important differences may be overlooked; if too fine-grained, statistical power is lost and results become unwieldy. Here, we introduce Latent Embedding Multivariate Regression (LEMUR), which enables differential expression analysis using a continuous low-dimensional latent space representation of cell type and state diversity, and thus operates without, or before, commitment to discrete categorization. LEMUR (1) aligns data from the different conditions, (2) predicts how each cell's gene expression would change as a function of the conditions and its position in latent space, and (3) for each gene, identifies compact neighborhoods of cells with consistent differential expression. Unlike statically defined clusters, these neighborhoods adapt to the underlying gene expression changes. We validate the method on a compendium of single-cell datasets and show applications to the identification of tumor subpopulations with distinct drug responses, the interplay between cell state and developmental time in zebrafish embryos, and the discovery of cell state × environment interactions in a spatial single-cell study of plaques in Alzheimer's disease. LEMUR is broadly applicable as a first-line analysis approach to multi-condition sc-RNA-seq data.
Software availability: `https://bioconductor.org/packages/lemur`
Contact: constantin.ahlmann@embl.de

Premature discretization of continuous variables leads to artifacts in data analysis and a loss of power; yet, it is the dominant approach to deal with the cell state diversity in multi-condition single-cell data. Lähnemann et al. (2020) described overcoming the reliance on clustering or cell type assignment before downstream analysis as one of the grand challenges in single-cell data analysis. Single-cell RNA-seq can be used to study the effect of experimental interventions or observational conditions on a heterogeneous set of cells, e.g., from tissue biopsies or organoids. Typically, cells from the same sample share the same condition but come from multiple cell types and states (e.g., position in a differentiation or cellular aging path, cell cycle, metabolism). Compared to bulk-sequencing, the novelty of multi-condition single-cell RNA-seq is the ability to disentangle expression changes between corresponding cells (i.e., same cell type and state) under different conditions, from those between cell types or states.

Here, we present a unified approach to address three tasks in multi-condition single-cell data analysis: (1) integrate the data into a common latent space, (2) for each cell, predict the expression it would have in any of the conditions, and (3) for each gene, find sets of cells which show similar differential expression of that gene.

Several methods exist for task (1), with the

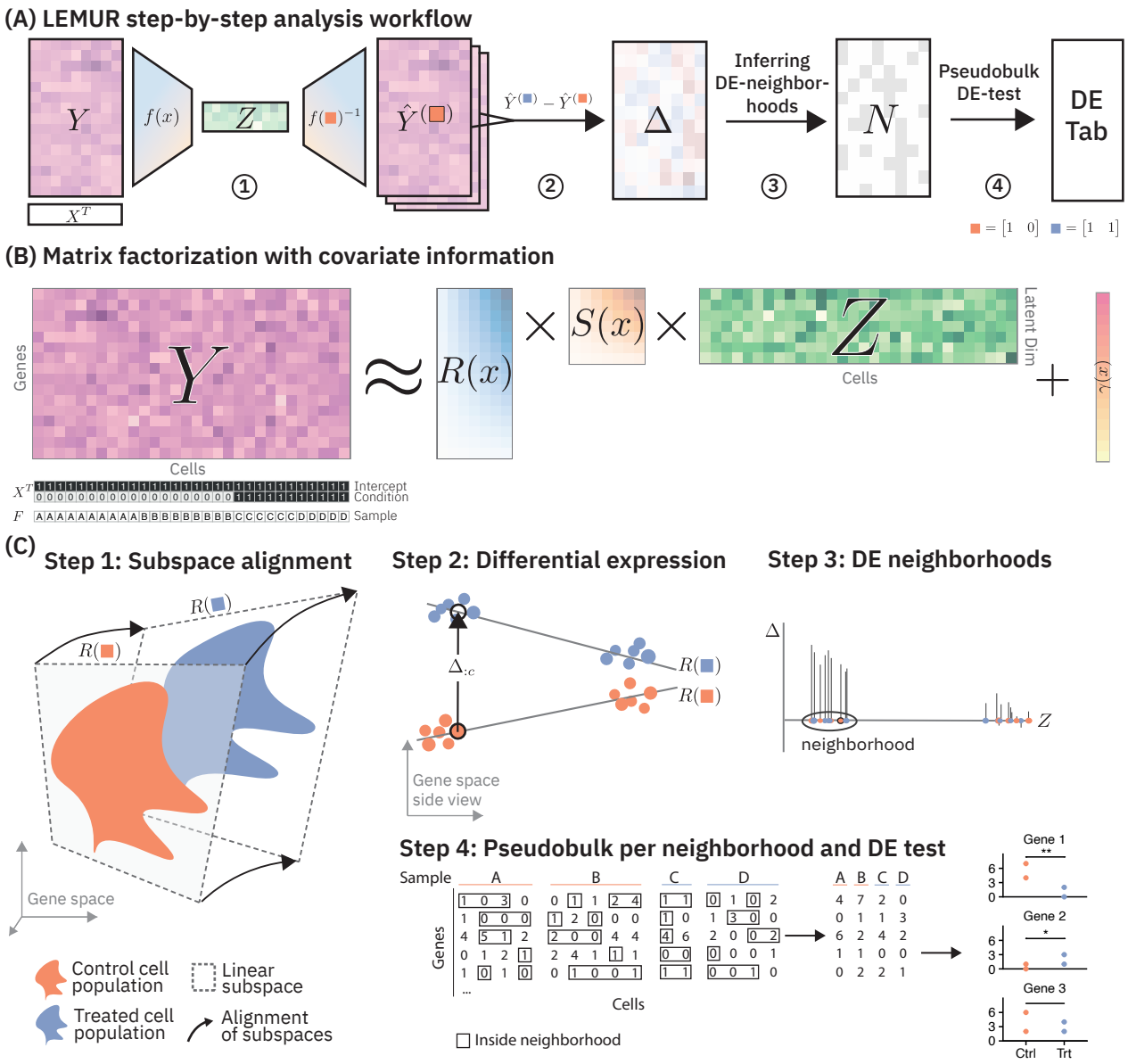

Figure 1 | Conceptual overview of latent embedding multivariate regression (LEMUR). (A) Four-step workflow. (B) The matrix factorization at the core of LEMUR. (C) Details on each step from (A): (1) A linear subspace is fitted separately for each condition. The subspaces for the different conditions are related to each other via rigid transformations that are parameterized by the covariates. (2) The differential expression statistic Δ is computed as the difference between the predicted values in the control and treated condition. (3) Cells close to each other with consistent Δ values are grouped into neighborhoods. (4) The pseudobulked differential expression test contrasts the summed counts from the cells inside the neighborhood per sample.

more or less explicit aim that the variation remaining in the common latent space represents cell type or cell state, and no longer the external conditions (Korsunsky et al., 2019; Haghverdi et al., 2018; Butler et al., 2018; Lopez et al., 2018). A smaller number of tools can also predict for a cell observed in one condition what its expression would have been, had it been in any of the other conditions (Lotfollahi et al., 2019, 2023; Bunne et al., 2023). scGEN, CPA, and CellOT achieve this by inverting the embedding function using an autoencoder model. Other integration methods, including Harmony, map the data to the common embedding space simply by enumerating the mapped coordinates for all observed cells, and thus have no canonical way to ask that useful counterfactual.

For differential expression analysis, state-of-

the-art methods take an integrated embedding, discretize it into (potentially overlapping) "clusters", and run a pseudobulked differential expression test for each cluster separately (Crowell et al., 2020; Missarova et al., 2023). Here, we employ LEMUR's counterfactual predictions to compute differential expression statistics for each gene and cell, and then select connected sets of cells with consistent differential expression. To achieve this, we decompose the variation in the data into four sources:

1. the conditions, which are explicitly known,
2. cell types or states that are not explicitly known, but assumed to lie on a low-dimensional manifold,
3. interactions between the two, and
4. unexplained residual variability.

We call our method Latent Embedding MUltivariate Regression (LEMUR). The method implements a new parametric model to find a suitable mapping from sc-RNA-seq data space to the latent representation. We use this mapping to predict the gene expression counterfactual. The method is implemented in an `R` package on Bioconductor called *lemur*.

Results

Figure 1A outlines LEMUR's workflow. The method takes as input a data matrix Y of size $G \times C$, where G is the number of genes and C is the number of cells. It assumes that appropriate preprocessing, including size factor normalization and variance stabilization was performed (Ahlmann-Eltze and Huber, 2023). In addition, it expects two tables of metadata for the cells: the vector F of length C which for each cell specifies the sample (independent experimental unit, e.g., tissue biopsy or organoid) it originates from, and the $C \times K$ design matrix X(Law et al., 2020). The design matrix encodes covariates that represent experimental treatments and/or observational conditions. It is analogous to the design matrix in differential expression tools like limma (Smyth, 2004) and DESeq2 (Love et al., 2014) and can account for fully general experimental or study designs. We term a unique combination of covariate values a *condition* and, for the differential expression testing, aggregate the data by condition and sample. Optionally, "landmark information" may be provided in the form of sets of cells from different conditions that are meant to correspond to each other. This information can either be explicitly provided by the user, for example, in the form of cell type labels, or it can be computationally inferred by methods such as Harmony's maximum diversity clustering (details in Methods).

LEMUR produces the following outputs:

- a common low-dimensional latent space representation of all cells from all conditions in $\mathbb{R}^P$, where the coordinates of the cells are given by the $P \times C$ dimensional matrix Z,
- a parametric family of bijective linear transformations f that map the condition-specific P-dimensional latent spaces into each other, and into the common space $\mathbb{R}^P$,
- the predicted expression $\hat{Y}$ for each gene and cell in any condition,
- the predicted difference Δ for each gene and cell, for the contrast between any pair of conditions,
- for each gene and contrast, a neighborhood of cells and a statistical measure of significance. The intention for these neighborhoods is to be connected, convex, and maximal, i.e., the differential expression pattern would become disproportionately less consistent and less significant if the neighborhood were extended.

The last of these will usually be the one end users care about most; the others are useful for diagnostics, quality assessment, visualization, and further modeling uses of the data. The explicit parameterization of the transformations f means that they can easily be inter- or extrapolated beyond the observed set of data, and inverted from the low-dimensional embedding back to the data space. In this sense, LEMUR is also a generative model.

Matrix factorization in the presence of known covariate information

The central idea of LEMUR is a multi-condition extension of principal component analysis (PCA) (Fig. 1B). We begin by setting up the building blocks. PCA (and similarly SVD) can be used to approximate a data matrix Y by a product of two smaller matrices

$$Y \approx RZ + \gamma_{\text{offset}}. \tag{1}$$

Here, R is a $G \times P$ matrix whose columns are called principal vectors (or sometimes rotation or loadings matrix) and describes the linear subspace that best explains the variation in Y. The principal vectors are orthonormal ($R^T R = I_P$). The $P \times C$ embedding matrix Z contains the P-dimensional coordinates of each cell in the latent space. γ_{offset} is a column vector of length G and centers the observations[1]. The value of P controls the expressiveness of the model. We are interested in the case $P \ll \min(G, C)$.

What is missing from model (1) is an ability to encode explicitly known experimental or study covariates. LEMUR adds this capability by adding a regression analysis component.

Covariates are encoded in the $C \times K$ design matrix X. For instance, in the simple case of a two-condition comparison, $K = 2$ and X is a two-column matrix, whose elements are all 1 in the first column (intercept) and 0 or 1 in the second column, indicating for each cell which condition it is from. We generalize (1) by treating R as a function of the rows of X (Fig. 1B),

$$R : \mathbb{R}^K \to \{U \in \mathbb{R}^{G \times P} \mid U^T U = I_P\}. \quad (2)$$

Thus, R maps for each cell c its covariates $X_{c:}$ to an orthonormal $G \times P$ matrix $R(X_{c:})$, and the model is

$$Y_{:c} \approx R(X_{c:})\, Z_{:c} + \gamma(X_{c:}). \quad (3)$$

Here, we use the notation : to indicate extracting row or column vectors from a matrix (e.g., $Z_{:c}$ is a vector of length P that contains the latent space representation of cell c). We allow the offset γ to depend on the covariates, too. The details of the parametrization are explained in the Methods.

Model (3) addresses the variance decomposition task posed in the introduction: known sources of variation are encoded in the design matrix X, which is explicitly specified; cell type and state variations take place in Z, which is latent, i.e., needs to be estimated from data. The term $\gamma(X_{c:})$ models expression changes associated with the different conditions that equally affect all cells. The term $R(X_{c:})$ captures expression changes associated with each condition that differently affect different cell types or states, i.e., different directions in latent space. It is analogous to an interaction term in ordinary linear regression. Unexplained variability is absorbed by the residuals of the approximation.

The mapping R aligns the subspaces of all conditions (Fig. 1C, step 1); however, these transformations are rigid and isometric. In some applications, we noted a need for more flexibility. For instance, consider a biological system with two cell types that are differently affected by a drug treatment. In such a case, the centers of the two cell populations might "move apart" under the treatment. To allow for such situations, we extend model (3) with the non-isometric, affine linear transformation S

$$Y_{:c} \approx R(X_{c:})\, S(X_{c:})\, Z_{:c} + \gamma(X_{c:}). \quad (4)$$

If landmarks are provided, the function $S(X_{c:})$ is fitted to satisfy them while staying as close as possible to the identity matrix I_P. Otherwise, $S \equiv I_P$.

Cluster-free differential expression analysis

We can predict the expression of cell c in any condition using the parametric model Eqn. (4). The differential expression between two conditions (Fig. 1C, step 2) is just the difference between their predictions. In formulæ,

$$\begin{aligned} \hat{Y}^{(1)}_{:c} &= R(d_1)\, S(d_1)\, Z_{:c} + \gamma(d_1) \\ \hat{Y}^{(2)}_{:c} &= R(d_2)\, S(d_2)\, Z_{:c} + \gamma(d_2) \\ \Delta_{:c} &= \hat{Y}^{(2)}_{:c} - \hat{Y}^{(1)}_{:c}, \end{aligned} \quad (5)$$

where d_1 is the row of the design matrix for the first condition and d_2 that for the other condition. $\hat{Y}^{(1)}_{:c}$ and $\hat{Y}^{(2)}_{:c}$ are the two predictions. Their difference $\Delta_{:c}$ can be computed for each cell—even though for any cell, data were only observed in exactly one replicate of one condition.

The resulting $G \times C$ matrix of differential expression estimates Δ has two uses: first, we visualize the differential expression values for selected genes as a function of latent space. In practice, we produce such visualizations using a non-linear 2D embedding of the P-dimensional latent space with, e.g., UMAP (McInnes et al., 2018). We show examples in Figs. 2 and 3. Second, we use Δ to guide the identification of differential expression neighborhoods, i.e., groups of cells that consistently show differential expression for a particular gene (Fig. 1C, step 3).

[1] We use a recycling convention like the one used in the R language for the sum operator (+) for a matrix A and a conformable column vector b: $(A + b)_{ij} = A_{ij} + b_i$

We do not attempt to quantify the statistical uncertainty associated with any particular value Δ_{gc}, due to the complicated correlation structure of Model (4). Instead, we use pseudobulk aggregation (Crowell et al., 2020) followed by glmGamPoi (Ahlmann-Eltze and Huber, 2020) or edgeR (Robinson et al., 2010) as a simple and effective approach to differential expression testing. For each sample, we sum up the counts of the cells in the neighborhood to obtain a neighborhood-specific genes × samples count table (Fig. 1C, Step 4).

Analysis of a treatment/control experiment: panobinostat in glioblastoma

Zhao et al. (2021) reported single-cell RNA-seq data of glioblastoma biopsies. Aliquots from five patients were assayed in two conditions: control and panobinostat, a histone deacetylase (HDAC) inhibitor (Fig. 2A). After quality control, the data contained 65 955 cells (Suppl. Tab. S1).

The left column of Fig. 2B shows a two-dimensional UMAP visualization of the input data Y. Most visible variation is associated with the known covariates: donor and treatment condition. Some further variation is related to the different cell types in the biopsies. We used LEMUR to absorb donor and treatment effects into R, setting the latent space dimension to $P = 60$. The middle column of Fig. 2B shows, upon fixing $S(x) = I$, a UMAP of the resulting matrix Z of latent coordinates for each cell. Cells from different samples are more intermixed, and within-sample cellular heterogeneity becomes more evident. This picture became even clearer after we used S to encode an alignment between cell subpopulations across samples using Harmony's maximum diversity clustering (Fig. 2B, right column). Here, a large population of tumor cells and three non-tumor subpopulations became apparent. The expression of selected marker genes is shown in the upper panel of Fig. 2C. The lower panel of Fig. 2C shows the ratio of average gene expression on chromosome 7, resp. 10, over the average expression on chromosomes 1-5, verifying the tumor cells' identification, as they are known to bear an amplification of chromosome 7 and a deletion of chromosome 10 (Zhao et al., 2021).

LEMUR's latent space is readily interpretable due to its affine-linear relationship to the original data space. This is exemplified in Figure 2D, which extends the biplot concept from PCA (Gabriel, 1971) to the multi-condition setting. The points show the first two coordinates of Z for all cells. Superimposed arrows show how expression changes affect the position in latent space. The upper panel does this for three cell type marker genes (*CD14*, *PLP1*, *GAP43*), whose arrows point toward their associated cell type in both conditions. In the lower panel, the arrows for *HIST3H2A* differ between control and panobinostat in line with a cell type-specific up-regulation of this gene.

Using LEMUR's differential expression testing, we found that panobinostat caused cell population-specific expression changes in 25% of all genes (2 498 of 10 000) at an FDR of 10%. Fig. 2E shows the result for *HIST3H2A*, highlighting up-regulation mostly in myeloid cells. Results for six other genes and the underlying expression values are shown in Suppl. Fig. S1.

We identified subpopulations of tumor cells that differentially responded to panobinostat treatment (Fig. 2F, Suppl. Fig. S1). In a subpopulation of 9 430 tumor cells, treatment with panobinostat caused downregulation of *LMO2*, while in the majority of tumor cells ($n = 36\,535$) expression of *LMO2* was unchanged (Fig. 2F, right panel). *LMO2* forms protein complexes with the transcription factors *TAL1*, *TCF3*, and *GATA*; it is important for angiogenesis and was originally discovered as an oncogene in T cell acute lymphoblastic leukemia (T-ALL) (Chambers and Rabbitts, 2015). Kim et al. (2015) studied the role of *LMO2* in glioblastoma and found that higher expression is associated with worse patient survival. They concluded that *LMO2* could be a clinically relevant drug target. To further characterize the group of cells where panobinostat downregulates *LMO2*, we compared the gene expression of the cells inside the neighborhood in the control condition against the other tumor cells in the control condition. We found a down-regulation of ribosomal genes indicating that the responding cells are less translationally active (Fig. 2G).

Analysis of a time course: zebrafish embryo development

Saunders et al. (2023) reported an atlas of zebrafish embryo development comprising 967 embryos and 838 036 cells collected at 16 time points between 18h and 48h post fertilization (Fig. 3A).

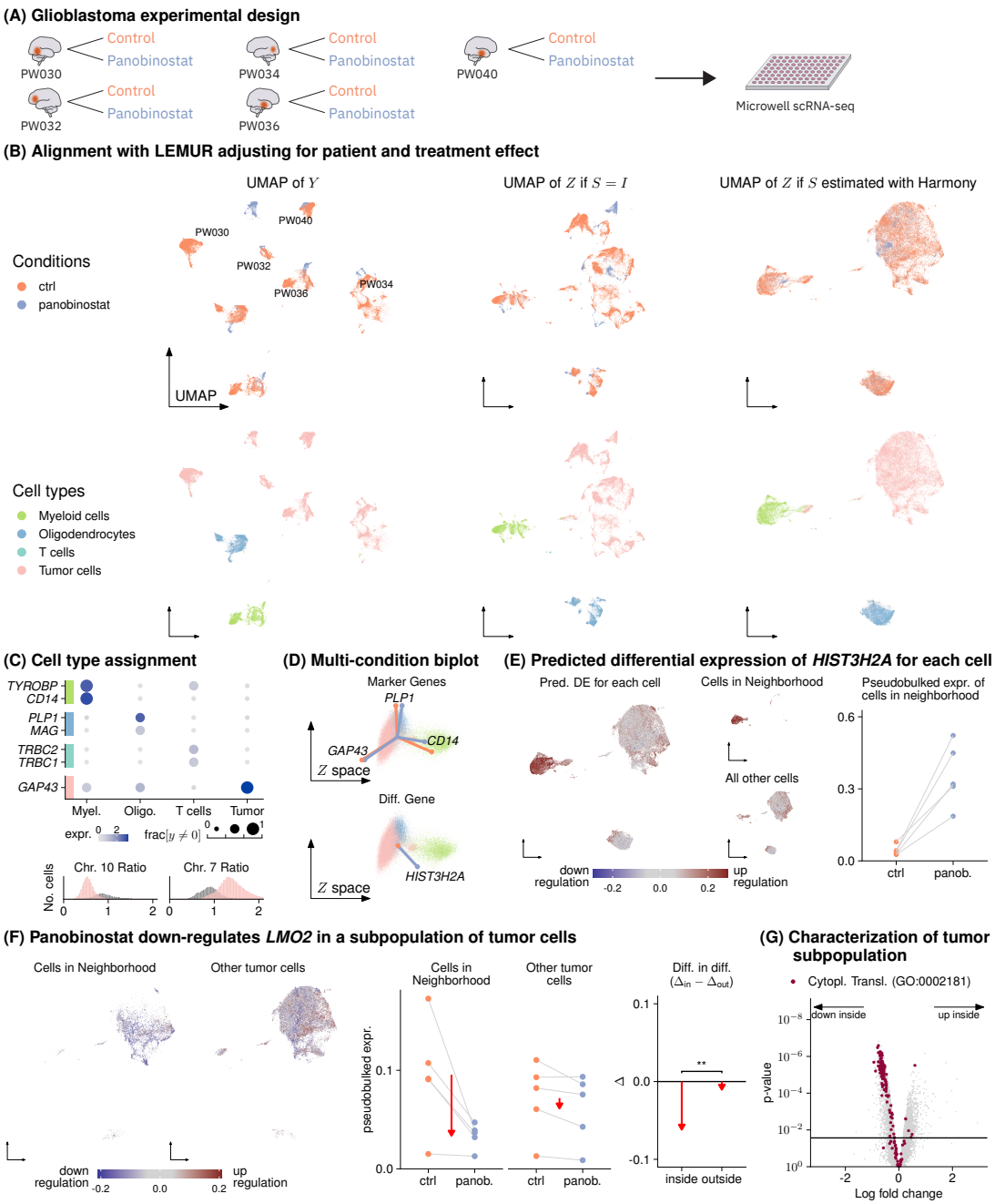

Figure 2 | Analysis of five glioblastoma tumor biopsies. (A) Experimental design. (B) UMAP plots of the log-transformed data (first column) and the latent embeddings produced by LEMUR (second and third column), colored by treatment and cell type (first and second row, respectively). (C) Marker gene and chromosome-aggregated expression levels for each cell type (grey densities are the non-tumor cell types). (D) Multi-condition biplots showing the first two dimensions of LEMUR's latent space (Z) for all cells. Top panel: arrows representing three cell type marker genes from Panel C; bottom panel: a gene with large expression change specifically in myeloid cells (*HIST3H2A*). (E) UMAP plots with cells colored by predicted expression change. The faceted plot splits the cells inside and outside the neighborhood. The scatter plot on the right shows the pseudobulked expression values from cells inside the neighborhood by donor and condition. (F) Differential expression analysis of *LMO2* within the tumor cells. Faceted UMAP plot of the cells inside and outside the neighborhood. The scatter plots in the middle show the pseudobulked expression values from cells inside and outside the neighborhood by donor and condition. The panel on the right compares the differences inside and outside the neighborhood (red arrows). (G) Volcano plot for the comparison between cells in- and outside the subpopulation from panel F, all in the control condition. Gene set enrichment analysis points to reduced translation activity in the subpopulation.

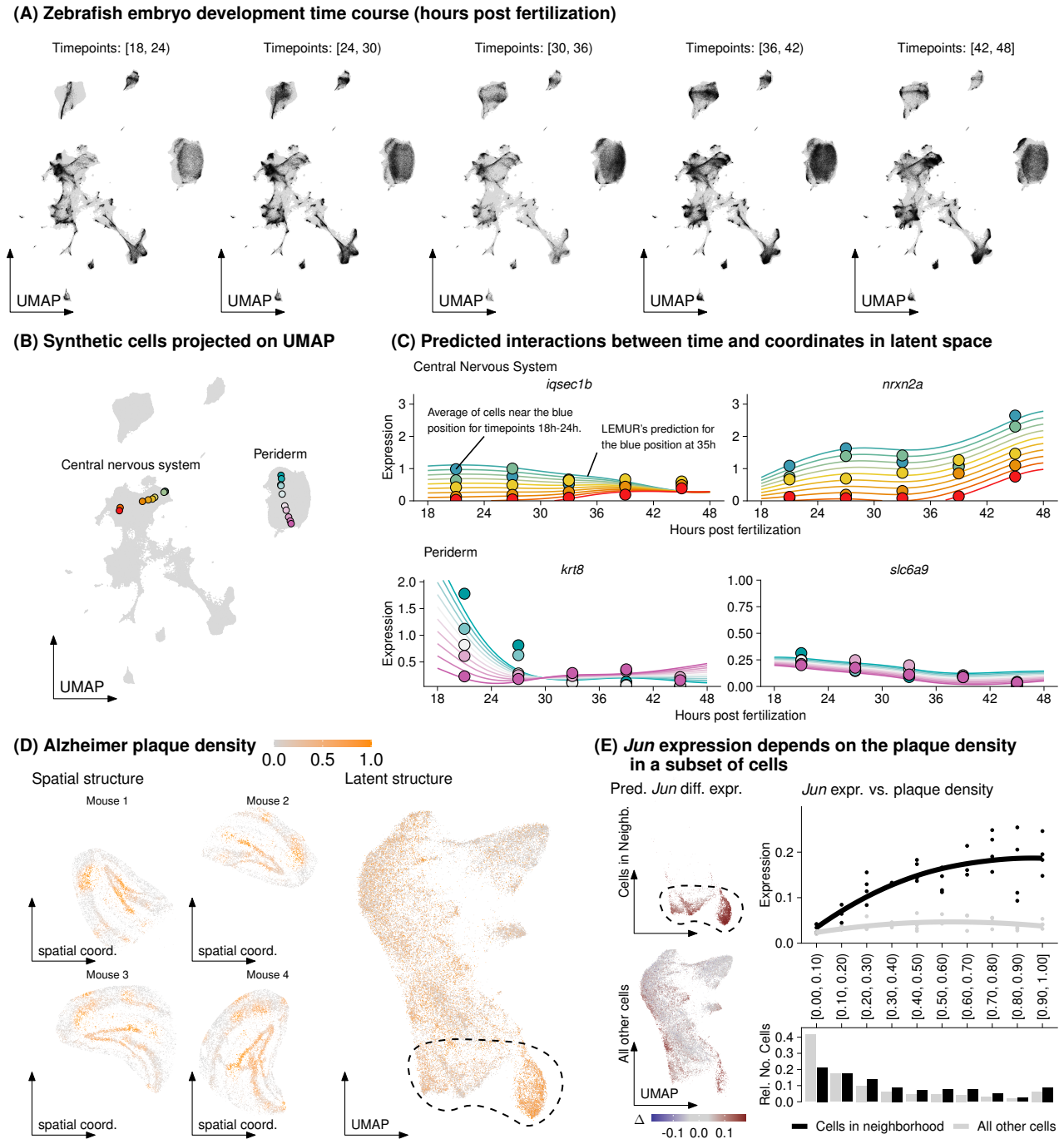

Figure 3 | Analysis of a time course and a spatial single-cell experiment (A) UMAP plots of embryonic development based on LEMUR's integrated latent space. In black are the cells from the respective hours post fertilization bracket, and in grey are all cells for comparison. (B) Position of synthetic cells (colored) projected on the UMAP of the full dataset (grey). The synthetic cells interpolate between the positions of two periderm and two central nervous system cells, respectively. (C) Line and dot plot for four genes showing their smooth expression predictions (lines) and the averaged observed data (points) as a function of time (x-axis) and latent space coordinates (color). (D) Spatial and UMAP plots of the cells from the hippocampi of four mice colored by Alzheimer's plaque density. (E) Left panels: Predicted expression change between the smallest and highest plaque density bracket. The dashed line encloses cells inside the differential expression neighborhood for *Jun*. Right top panel: Scatter plot of *Jun* expression as a function of plaque density for cells inside the neighborhood and all other cells. The line is a LOESS fit. The bottom right panel: the relative number of cells per plaque density bin.

We used natural cubic splines to model the time dependence, following Smyth et al. (2023). The UMAPs are based on LEMUR's integrated latent space; however, we do *not* expect perfect overlap of the cells across all time points, since some cell types only exist at particular stages of development.

We wanted to find gene expression interactions between developmental time and the cell state within a cell type. For this, we used LEMUR's ability to predict the expression at any point in latent space across time. We generated synthetic cells by linearly interpolating the position in the latent space Z for two cells from the periderm (purple and turquoise) and two cells from the central nervous system (red and green) (Fig. 3B, Suppl. Fig. S2A).

For four genes, we compared the predictions for the synthetic cells over time with the observed expression of the nearest neighbors in each 6-hour interval (Fig. 3C) and demonstrated that LEMUR can disentangle the interaction between the developmental time and the latent position. We find, for example, that *krt8* shows a decreasing expression pattern over time for cells close to the blue cell and increasing expression for cells close to the purple cell, indicating cell state-specific temporal gene regulation within the periderm (Suppl. Fig. S3).

Analysis of spatially-resolved expression: plaque density in Alzheimer's disease

Cable et al. (2022) performed Slide-seq V2 on the hippocampus of four mice genetically engineered to model amyloidosis in Alzheimer's disease. Using microscopy, they quantified the spatial density of Aβ plaques (Fig. 3D). Thus, plaque density is an observational covariate that varies from cell to cell; this is in contrast to covariates considered above, which vary from sample to sample. Cable et al. (2022) reported a differential expression analysis per discrete cell type category; however, such categorization is not easy to justify given the gradual composition suggested by the data (Fig. 3D right panel, Suppl. Fig. S2B). LEMUR enabled us to skip cell type categorization and directly look for genes whose expression varied between low and high plaque density in adaptively found subsets of cells. Fig. 3E shows the differential expression prediction for *Jun*, a transcription factor that was identified as a member of the pathway regulating β amyloid-induced apoptosis (Morishima et al., 2001; Akhter et al., 2015). Here we show that a higher plaque density was correlated with increased expression of *Jun* only in the circled subset but not all cells (Fig. 3E).

Performance validation

We validated the performance and reliability of LEMUR using 13 publicly available multi-condition single-cell datasets. We preprocessed each dataset consistently following Ahlmann-Eltze and Huber (2023).

The goal of integration methods is to find a low-dimensional representation in which the known covariates are considered a nuisance ("batch effects") and no longer cause notable variation, while latent variability is meant to represent biological signal ("cell type") and is retained. In Figure 4A, we illustrate this on a dataset of Lupus patient samples treated with vehicle control or interferon-β (Kang et al., 2018). We quantify the first goal by counting for each cell how many of its neighbors come from the same condition (k-nearest neighbor (k-NN) mixing). We quantify the second goal by comparing–for each condition separately–a clustering of the embedding with a clustering of the original data (adjusted Rand index (ARI)). An ideal method scores highly according to both metrics.

Across the thirteen datasets, LEMUR's integration performance is similar to Harmony's, a popular tool for this task, and outperforms CPA on both measures (Fig. 4B). Suppl. Fig. S4 shows that the results are consistent across 7 additional metrics. It also shows that LEMUR with S fixed to the identity performs well in terms of signal retention but underperforms in the covariate neutralization.

LEMUR extends PCA, and thus, its performance in terms of variance explained for each additional latent dimension is very similar (Suppl. Fig. S6A). Similarly, LEMUR inherits the favorable runtime behavior of approximative PCA methods. For example, fitting PCA with 50 latent dimensions on the Goldfarbmuren data with 24 178 cells and 20 953 genes took us 35 seconds; for comparison, calculating LEMUR's multi-condition extension of PCA took 103 seconds (Suppl. Fig. S6B). Aligning the cells with landmarks or Harmony added 2 and 95 seconds, respectively. All these timings are negligible com-

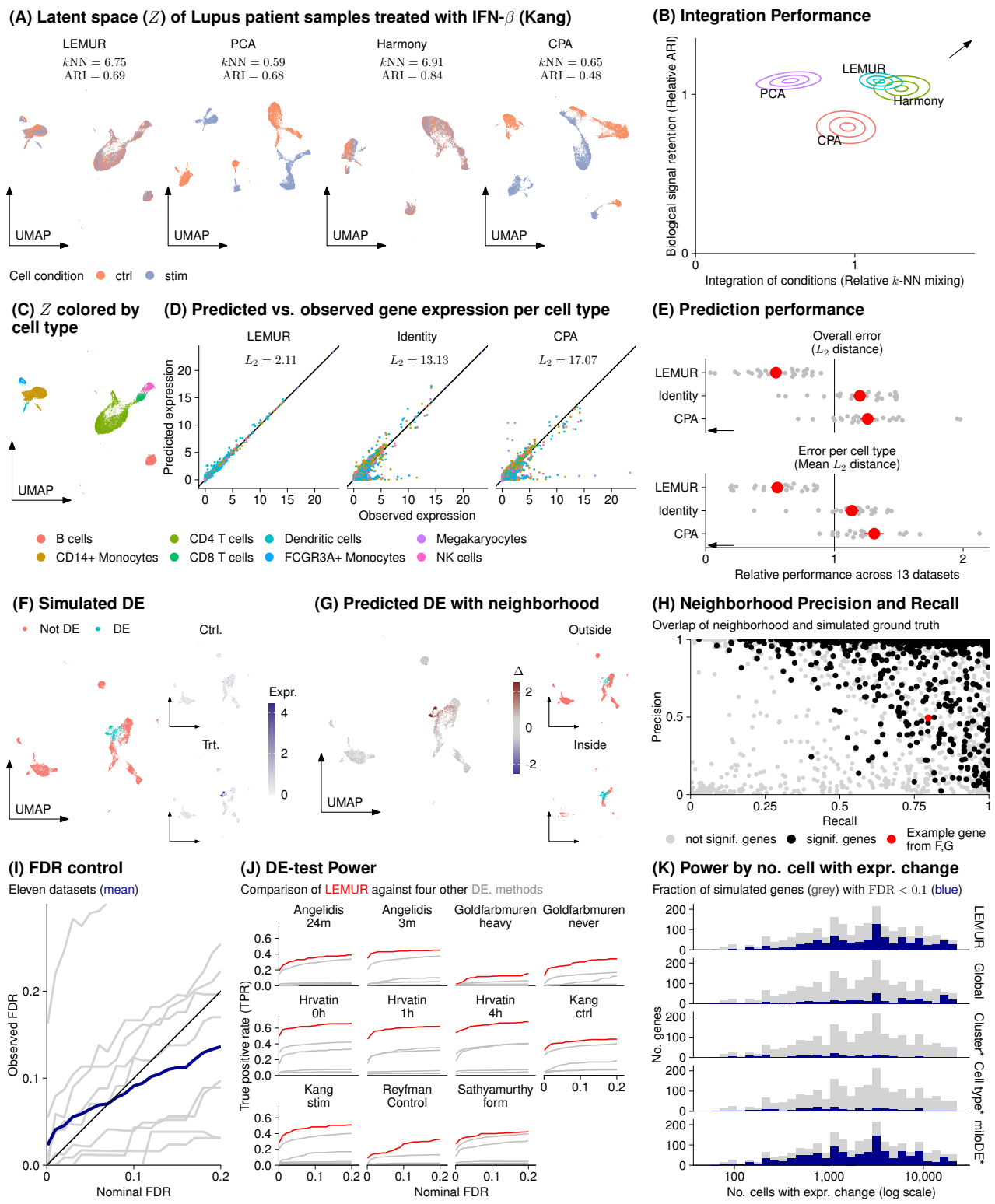

Figure 4 | Validation of LEMUR's performance. (A) UMAP plots of the latent space for the Kang dataset. The k-NN measures the adjustment for the known covariates, the ARI measure the biological signal retention. (B) Density plots of the bootstrapped mean performance for ARI and k-NN mixing across thirteen datasets. The values are normalized by the average performance per dataset. (C) UMAP of LEMUR's latent space colored by cell type. (D) Scatter plots of the treatment effect prediction against the observed expression values for a set of holdout cells from each cell type. (E) Aggregation of the prediction performance across thirteen datasets (grey points) with the overall mean (red point range).

Caption continues on next page.

Figure 4 continued (F) Large panel: UMAP of LEMUR's latent space where the color indicates if an expression change was simulated for that cell in the example gene. Small panels: the simulated expression values. (G) Large panel: predicted differential expression for the example gene from panel F ($\Delta = \hat{Y}^{\text{Trt}} - \hat{Y}^{\text{Ctrl}}$). Small panels: the set of cells inside or outside the inferred neighborhood. (H) Scatter plot of the precision and recall for each neighborhood with respect to the simulated ground truth. (I) Line plot comparing the nominal FDR and the observed FDR for eleven datasets (grey) with the overall mean (blue). (J) Line plot for each dataset showing the true positive rate against the nominal FDR. (K) Histogram of the number of cells for which a differential expression was simulated across all datasets. In blue is the fraction of genes detected as significant for each method. For the methods that conducted multiple tests per gene (highlighted with *), we only considered the minimum FDR per gene.

pared to analysts' overall effort.

Then, we validated LEMUR's capability to predict gene expression across conditions. We predicted the gene expression under treatment for cells originally observed in the control condition, and compared the predictions to the observed expression values in actually treated cells. As we cannot directly link individual observed cells between conditions, we averaged the observed and predicted expression per cell type. Fig. 4D shows the results for the Kang dataset for eight cell types (Fig. 4C) and 500 genes. Summing up the distances between observed and predicted values is a useful measure for prediction performance. Here, smaller values indicate better performance.

Across the thirteen datasets, LEMUR accurately predicts the gene expression and outperforms CPA in terms of overall error and error per cell type (Fig. 4E). Suppl. S5 shows that the results are consistent across 6 additional metrics. It also shows that using a fixed latent space R (instead of LEMUR's $R(x)$) or using $S = I$ (instead of estimating S with Harmony) performs worse than the full LEMUR model.

Next, we quantified LEMUR's ability to identify neighborhoods of cells with consistent differential expression. Fig. 4F shows the differential expression pattern for one gene in the Kang dataset. We implanted a gene with high expression for one cell cluster (Fig. 4F right column). Fig. 4G shows that LEMUR accurately identified the corresponding expression changes and inferred a neighborhood that overlapped well with the simulated ground truth. Fig. 4H shows the overlap of the inferred neighborhoods with the cells, that have an expression change (DE-cells) for all simulated genes from the Kang dataset.

Last, we show that LEMUR's differential expression test controls the false discovery rate (FDR) across eleven semi-synthetic datasets (Fig. 4I, details in Methods). LEMUR is more powerful than a pseudobulked test across all cells (*global*) or separate tests for subsets of cells (either by *cell type* or *cluster* as in Crowell et al. (2020), or by neighborhood as in *miloDE* (Missarova et al., 2023)) (Fig. 4J). Suppl. Fig. S7 assesses FDR control and power for all methods and some additional variants of LEMUR. It shows that accounting for the post-selection bias from the neighborhood inference is important, and that it is successfully addressed by LEMUR's data splitting. Fig. 4K shows the power of each differential testing approach stratified by the number of cells with an expression change at FDR = 0.1. It shows that relative to the cluster and cell type-based tests, LEMUR identifies more large-scale differential expression patterns.

Discussion

Latent embedding multivariate regression (LEMUR) enables differential expression analysis of single-cell resolution expression data between complex samples, such as tissue biopsies, organs, organoids or whole organisms. The method allows for arbitrary experimental or study designs, specified by a design matrix, just as in ordinary linear regression. Applications range from comparisons between two conditions with replicates, over paired studies, such as a series of tissue biopsies before and after treatment, over studies with multiple covariates (e.g., genetic and drug perturbations), interactions between covariates, and continuous covariates. The method represents cell-to-cell variation within a condition using a continuous latent space. Thus, it avoids—or postpones—the need for categorical assignment of cells to discrete

cell types or cell states, and offers a solution to one of the challenges posed by Lähnemann et al. (2020).

We demonstrated the utility of the approach on three prototypical applications, and we benchmarked important aspects of its performance on a compendium of 13 datasets. The application cases are a matched control-treatment study of patient samples in glioblastoma, an atlas of Zebrafish embryo development where time is a continuous covariate, and a spatial transcriptomics study of Alzheimer's plaques where plaque density is a continuous covariate. We showed how LEMUR identified biologically relevant cell subpopulations and gene expression patterns.

To achieve this, we combine latent space representation by dimension reduction with regression analysis in a novel matrix factorization approach. The model is predictive: for any observed cell, it predicts its gene expression in any of the conditions, even though each cell was only observed exactly once. Moreover, as each cell is parameterized by a position in P-dimensional real space, the model can also predict the expression of "synthetic cells" at unobserved positions, say in between observed cells or extrapolating out, in any condition. We use these capabilities for differential expression analysis.

Furthermore, we infer neighborhoods of cells with consistent differential expression patterns with respect to comparisons ("contrasts") of interest. The neighborhoods are found in a data-driven manner. No a priori categorization of cells into "cell types" is needed, but once neighborhoods have been identified, one can annotate or compare them with cell type or cell state markers or annotations.

Our current implementation of the neighborhood finding leaves obvious room for future improvements. It is stochastic, by relying on a random sample of one-dimensional projections of point clouds in P-dimensional space. Thus, repeated running of the algorithm can result in (slightly) different outputs. Also, it addresses the post-selection inference problem using a rather heavy-handed data splitting approach.

Unlike other single-cell data integration and expression prediction tools, LEMUR is built around linear methods, and the model is analytically parameterized with a modest number of parameters and a small number of layers. This is in contrast to the often-repeated claim that the complicatedness of single-cell data necessitates non-linear methods and 'deep' models. We showed that our approach based on simple, linear matrix decomposition using a sufficiently high-dimensional latent space is capable of representing the data in a useful manner. Compared to deep-learning approaches, LEMUR's interpretable, simple, and easy-to-inspect model should facilitate follow-up investigation of its discoveries.

Overall, we believe that LEMUR is a valuable tool for first-line analysis of multi-condition single-cell data. Compared to approaches that require discretization into clusters or groups before differential expression analysis, representing cell types and states in a continuous latent space may better fit the underlying biology, and may facilitate the precise identification of affected cells. This in turn should ease analysts' work, and enable biological discoveries that could otherwise be missed.

Availability

All datasets used in this manuscript are publicly available:

Dataset	Availability
Angelidis et al. (2019)	GSE124872
Aztekin et al. (2019)	bioc::scRNAseq
Bunis et al. (2021)	bioc::scRNAseq
Goldfarbmuren et al. (2020)	GSE134174
Hrvatin et al. (2018)	GSE102827
Jäkel et al. (2019)	GSE118257
Sathyamurthy et al. (2018)	GSE103892
Kang et al. (2018)	Zenodo 4473025
Bhattacherjee et al. (2019)	Zenodo 4473025
Skinnider et al. (2021)	Zenodo 4473025
Cano-Gamez et al. (2020)	Zenodo 5048449
Reyfman et al. (2019)	Zenodo 5048449
Pijuan-Sala et al. (2019)	bioc::Mouse GastrulationData
Zhao et al. (2021)	GSE148842
Saunders et al. (2023)	GSE202639
Cable et al. (2022)	SCP1663

The *lemur* `R` package is available at bioc::lemur and the code to reproduce the analysis is available at github.com/const-ae/lemur-Paper.

Acknowledgments

We thank Dr. Simon Anders, Dr. Oliver Stegle, and Dr. Judith Zaugg for valuable feedback and discussions. We thank Dr. Ronny Bergmann for his advice on optimization on manifolds. We thank Dr. Lauren Saunders for early access to and discussion of the zebrafish data. We thank EMBL IT services and HPC resources for providing the infrastructure to perform the computations needed for this work. We thank the EMBL Kinderhaus for excellent childcare while WH was working on this project.

Funding

This work has been supported by the EMBL International Ph.D. Programme, by the German Federal Ministry of Education and Research (CompLS project SIMONA under grant agreement no. 031L0263A), and the European Research Council (Synergy Grant DECODE under grant agreement no. 810296).

References

Absil, P.-A., Mahony, R. and Sepulchre, R. (2004). Riemannian geometry of Grassmann manifolds with a view on algorithmic computation. *Acta Applicandae Mathematica* 80: 199–220, doi: 10.1023/B:ACAP.0000013855.14971.91.

Ahlmann-Eltze, C. and Huber, W. (2020). glmGamPoi: fitting Gamma-Poisson generalized linear models on single cell count data. *Bioinformatics* 36: 5701–5702, doi: 10.1093/bioinformatics/btaa1009.

Ahlmann-Eltze, C. and Huber, W. (2023). Comparison of transformations for single-cell RNA-seq data. *Nature Methods* 20: 665–672, doi: 10.1038/s41592-023-01814-1.

Akhter, R., Sanphui, P., Das, H., Saha, P. and Biswas, S. C. (2015). The regulation of p53 up-regulated modulator of apoptosis by JNK/c-Jun pathway in β-amyloid-induced neuron death. *Journal of Neurochemistry* 134: 1091–1103, doi: 10.1111/jnc.13128.

Angelidis, I., Simon, L. M., Fernandez, I. E., Strunz, M., Mayr, C. H., Greiffo, F. R., Tsitsiridis, G., Ansari, M., Graf, E., Strom, T.-M. et al. (2019). An atlas of the aging lung mapped by single cell transcriptomics and deep tissue proteomics. *Nature Communications* 10: 963, doi: 10.1038/s41467-019-08831-9.

Aztekin, C., Hiscock, T., Marioni, J., Gurdon, J., Simons, B. and Jullien, J. (2019). Identification of a regeneration-organizing cell in the xenopus tail. *Science* 364: 653–658, doi: 10.1126/science.aav9996.

Bendokat, T., Zimmermann, R. and Absil, P.-A. (2023). A Grassmann manifold handbook: Basic geometry and computational aspects. *arXiv* doi: 10.48550/arXiv.2011.13699.

Bhattacherjee, A., Djekidel, M. N., Chen, R., Chen, W., Tuesta, L. M. and Zhang, Y. (2019). Cell type-specific transcriptional programs in

mouse prefrontal cortex during adolescence and addiction. *Nature Communications* 10: 4169, doi: 10.1038/s41467-019-12054-3.

Bunis, D. G., Bronevetsky, Y., Krow-Lucal, E., Bhakta, N. R., Kim, C. C., Nerella, S., Jones, N., Mendoza, V. F., Bryson, Y. J., Gern, J. E. et al. (2021). Single-cell mapping of progressive fetal-to-adult transition in human naive T cells. *Cell Reports* 34, doi: 10.1016/j.celrep.2020.108573.

Bunne, C., Stark, S. G., Gut, G., Del Castillo, J. S., Levesque, M., Lehmann, K.-V., Pelkmans, L., Krause, A. and Rätsch, G. (2023). Learning single-cell perturbation responses using neural optimal transport. *Nature Methods* doi: 10.1038/s41592-023-01969-x.

Butler, A., Hoffman, P., Smibert, P., Papalexi, E. and Satija, R. (2018). Integrating single-cell transcriptomic data across different conditions, technologies, and species. *Nature Biotechnology* 36: 411–420, doi: 10.1038/nbt.4096.

Cable, D. M., Murray, E., Shanmugam, V., Zhang, S., Zou, L. S., Diao, M., Chen, H., Macosko, E. Z., Irizarry, R. A. and Chen, F. (2022). Cell type-specific inference of differential expression in spatial transcriptomics. *Nature Methods* 19: 1076–1087, doi: 10.1038/s41592-022-01575-3.

Cano-Gamez, E., Soskic, B., Roumeliotis, T. I., So, E., Smyth, D. J., Baldrighi, M., Willé, D., Nakic, N., Esparza-Gordillo, J., Larminie, C. G. et al. (2020). Single-cell transcriptomics identifies an effectorness gradient shaping the response of CD4+ T cells to cytokines. *Nature Communications* 11: 1801, doi: 10.1038/s41467-020-15543-y.

Chambers, J. and Rabbitts, T. H. (2015). LMO2 at 25 years: a paradigm of chromosomal translocation proteins. *Open Biology* 5: 150062, doi: 10.1098/rsob.150062.

Crowell, H. L., Soneson, C., Germain, P.-L., Calini, D., Collin, L., Raposo, C., Malhotra, D. and Robinson, M. D. (2020). Muscat detects subpopulation-specific state transitions from multi-sample multi-condition single-cell transcriptomics data. *Nature Communications* 11: 6077, doi: 10.1038/s41467-020-19894-4.

Cuomo, A. S., Heinen, T., Vagiaki, D., Horta, D., Marioni, J. C. and Stegle, O. (2022). CellRegMap: a statistical framework for mapping context-specific regulatory variants using scRNA-seq. *Molecular Systems Biology* 18: e10663, doi: 10.15252/msb.202110663.

Edelman, A., Arias, T. A. and Smith, S. T. (1998). The geometry of algorithms with orthogonality constraints. *SIAM Journal on Matrix Analysis and Applications* 20: 303–353, doi: 10.1137/S0895479895290954.

Gabriel, K. R. (1971). The biplot graphic display of matrices with application to principal component analysis. *Biometrika* 58: 453–467, doi: 10.2307/2334381.

Goldfarbmuren, K. C., Jackson, N. D., Sajuthi, S. P., Dyjack, N., Li, K. S., Rios, C. L., Plender, E. G., Montgomery, M. T., Everman, J. L., Bratcher, P. E. et al. (2020). Dissecting the cellular specificity of smoking effects and reconstructing lineages in the human airway epithelium. *Nature Communications* 11: 2485, doi: 10.1038/s41467-020-16239-z.

Gretton, A., Borgwardt, K. M., Rasch, M. J., Schölkopf, B. and Smola, A. (2012). A kernel two-sample test. *The Journal of Machine Learning Research* 13: 723–773.

Haghverdi, L., Lun, A. T., Morgan, M. D. and Marioni, J. C. (2018). Batch effects in single-cell RNA-sequencing data are corrected by matching mutual nearest neighbors. *Nature Biotechnology* 36: 421–427, doi: 10.1038/nbt.4091.

Hrvatin, S., Hochbaum, D. R., Nagy, M. A., Cicconet, M., Robertson, K., Cheadle, L., Zilionis, R., Ratner, A., Borges-Monroy, R., Klein, A. M. et al. (2018). Single-cell analysis of experience-dependent transcriptomic states in the mouse visual cortex. *Nature Neuroscience* 21: 120–129, doi: 10.1038/s41593-017-0029-5.

Jäkel, S., Agirre, E., Mendanha Falcão, A., Van Bruggen, D., Lee, K. W., Knuesel, I., Malhotra, D., Ffrench-Constant, C., Williams, A. and Castelo-Branco, G. (2019). Altered human oligodendrocyte heterogeneity in multiple sclerosis. *Nature* 566: 543–547, doi: 10.1038/s41586-019-0903-2.

Kang, H. M., Subramaniam, M., Targ, S., Nguyen, M., Maliskova, L., McCarthy, E., Wan, E., Wong, S., Byrnes, L., Lanata, C. M. et al. (2018). Multiplexed droplet single-cell RNA-sequencing using natural genetic variation. *Nature Biotechnology* 36: 89–94, doi: 10.1038/nbt.4042.

Kim, H. J., Adluru, N., Collins, M. D., Chung, M. K., Bendlin, B. B., Johnson, S. C., Davidson, R. J. and Singh, V. (2014). Multivariate

general linear models (MGLM) on Riemannian manifolds with applications to statistical analysis of diffusion weighted images. In *Proceedings of the IEEE Conference on Computer Vision and Pattern Recognition*, 2705–2712, doi: 10.1109/CVPR.2014.352.

Kim, S., Kim, E., Hitomi, M., Oh, S., Jin, X., Jeon, H., Beck, S., Kim, J., Park, C., Chang, S. et al. (2015). The lim-only transcription factor LMO2 determines tumorigenic and angiogenic traits in glioma stem cells. *Cell Death & Differentiation* 22: 1517–1525, doi: 10.1038/cdd.2015.7.

Korsunsky, I., Millard, N., Fan, J., Slowikowski, K., Zhang, F., Wei, K., Baglaenko, Y., Brenner, M., Loh, P.-r. and Raychaudhuri, S. (2019). Fast, sensitive and accurate integration of single-cell data with Harmony. *Nature Methods* 16: 1289–1296, doi: 10.1038/s41592-019-0619-0.

Lähnemann, D., Köster, J., Szczurek, E., McCarthy, D. J., Hicks, S. C., Robinson, M. D., Vallejos, C. A., Campbell, K. R., Beerenwinkel, N., Mahfouz, A. et al. (2020). Eleven grand challenges in single-cell data science. *Genome biology* 21: 1–35, doi: 10.1186/s13059-020-1926-6.

Law, C. W., Zeglinski, K., Dong, X., Alhamdoosh, M., Smyth, G. K. and Ritchie, M. E. (2020). A guide to creating design matrices for gene expression experiments. *F1000Research* 9: 1444, doi: 10.12688/f1000research.27893.1.

Li, G., Yang, D., Nobel, A. B. and Shen, H. (2016). Supervised singular value decomposition and its asymptotic properties. *Journal of Multivariate Analysis* 146: 7–17, doi: 10.1016/j.jmva.2015.02.016.

Lopez, R., Regier, J., Cole, M. B., Jordan, M. I. and Yosef, N. (2018). Deep generative modeling for single-cell transcriptomics. *Nature Methods* 15: 1053–1058, doi: 10.1038/s41592-018-0229-2.

Lotfollahi, M., Klimovskaia Susmelj, A., De Donno, C., Hetzel, L., Ji, Y., Ibarra, I. L., Srivatsan, S. R., Naghipourfar, M., Daza, R. M., Martin, B. et al. (2023). Predicting cellular responses to complex perturbations in high-throughput screens. *Molecular Systems Biology* : e11517doi: 10.15252/msb.202211517.

Lotfollahi, M., Wolf, F. A. and Theis, F. J. (2019). scGen predicts single-cell perturbation responses. *Nature Methods* 16: 715–721, doi: 10.1038/s41592-019-0494-8.

Love, M. I., Huber, W. and Anders, S. (2014). Moderated estimation of fold change and dispersion for RNA-seq data with DESeq2. *Genome biology* 15: 1–21, doi: 10.1186/s13059-014-0550-8.

Madrigal, A., Lu, T., Soto, L. M. and Najafabadi, H. S. (2023). A unified model for interpretable latent embedding of multi-sample, multi-condition single-cell data. *bioRxiv* doi: 10.1101/2023.08.15.553327.

McInnes, L., Healy, J. and Melville, J. (2018). UMAP: Uniform manifold approximation and projection for dimension reduction. *arXiv* doi: 10.48550/arXiv.1802.03426.

Missarova, A., Dann, E., Rosen, L., Satija, R. and Marioni, J. (2023). Sensitive cluster-free differential expression testing. *bioRxiv* doi: 10.1101/2023.03.08.531744.

Morishima, Y., Gotoh, Y., Zieg, J., Barrett, T., Takano, H., Flavell, R., Davis, R. J., Shirasaki, Y. and Greenberg, M. E. (2001). β-amyloid induces neuronal apoptosis via a mechanism that involves the c-Jun N-terminal kinase pathway and the induction of Fas ligand. *Journal of Neuroscience* 21: 7551–7560, doi: 10.1523/JNEUROSCI.21-19-07551.2001.

Nathan, A., Asgari, S., Ishigaki, K., Valencia, C., Amariuta, T., Luo, Y., Beynor, J. I., Baglaenko, Y., Suliman, S., Price, A. L. et al. (2022). Single-cell eQTL models reveal dynamic T cell state dependence of disease loci. *Nature* 606: 120–128, doi: 10.1038/s41586-022-04713-1.

Neufeld, A., Gao, L. L., Popp, J., Battle, A. and Witten, D. (2022). Inference after latent variable estimation for single-cell RNA sequencing data. *Biostatistics* doi: 10.1093/biostatistics/kxac047.

Pijuan-Sala, B., Griffiths, J. A., Guibentif, C., Hiscock, T. W., Jawaid, W., Calero-Nieto, F. J., Mulas, C., Ibarra-Soria, X., Tyser, R. C., Ho, D. L. L. et al. (2019). A single-cell molecular map of mouse gastrulation and early organogenesis. *Nature* 566: 490–495, doi: 10.1038/s41586-019-0933-9.

Reyfman, P. A., Walter, J. M., Joshi, N., Anekalla, K. R., McQuattie-Pimentel, A. C., Chiu, S., Fernandez, R., Akbarpour, M., Chen, C.-I., Ren, Z. et al. (2019). Single-cell transcriptomic analysis of human lung provides insights into the pathobiology of pulmonary

fibrosis. *American Journal of Respiratory and Critical Care Medicine* 199: 1517–1536, doi: 10.1164/rccm.201712-2410OC.

Robinson, M. D., McCarthy, D. J. and Smyth, G. K. (2010). edgeR: a Bioconductor package for differential expression analysis of digital gene expression data. *Bioinformatics* 26: 139–140, doi: 10.1093/bioinformatics/btp616.

Sathyamurthy, A., Johnson, K. R., Matson, K. J., Dobrott, C. I., Li, L., Ryba, A. R., Bergman, T. B., Kelly, M. C., Kelley, M. W. and Levine, A. J. (2018). Massively parallel single nucleus transcriptional profiling defines spinal cord neurons and their activity during behavior. *Cell Reports* 22: 2216–2225, doi: 10.1016/j.celrep.2018.02.003.

Saunders, A., Macosko, E. Z., Wysoker, A., Goldman, M., Krienen, F. M., Rivera, H. de, Bien, E., Baum, M., Bortolin, L., Wang, S. et al. (2018). Molecular diversity and specializations among the cells of the adult mouse brain. *Cell* 174: 1015–1030, doi: 10.1016/j.cell.2018.07.028.

Saunders, L. M., Srivatsan, S. R., Duran, M., Dorrity, M. W., Ewing, B., Linbo, T. H., Shendure, J., Raible, D. W., Moens, C. B., Kimelman, D. and Trapnell, C. (2023). Embryo-scale reverse genetics at single-cell resolution. *Nature* 623: 782–791, doi: 10.1038/s41586-023-06720-2.

Skinnider, M. A., Squair, J. W., Kathe, C., Anderson, M. A., Gautier, M., Matson, K. J., Milano, M., Hutson, T. H., Barraud, Q., Phillips, A. A. et al. (2021). Cell type prioritization in single-cell data. *Nature Biotechnology* 39: 30–34, doi: 10.1038/s41587-020-0605-1.

Smyth, G., Hu, Y., Ritchie, M., Silver, J., Wettenhall, J., McCarthy, D., Wu, D., Shi, W., Phipson, B., Lun, A., Thorne, N., Oshlack, A., Graaf, C. de, Chen, Y., Langaas, M., Ferkingstad, E., Davy, M., Pepin, F. and Choi, D. (2023). limma: linear models for microarray and RNA-seq data. doi: 10.18129/B9.bioc.limma, User guide (v3.58.1) chapter 9.6.2.

Smyth, G. K. (2004). Linear models and empirical bayes methods for assessing differential expression in microarray experiments. *Statistical Applications in Genetics and Molecular Biology* 3, doi: 10.2202/1544-6115.1027.

Zhao, W., Dovas, A., Spinazzi, E. F., Levitin, H. M., Banu, M. A., Upadhyayula, P., Sudhakar, T., Marie, T., Otten, M. L., Sisti, M. B. et al. (2021). Deconvolution of cell type-specific drug responses in human tumor tissue with single-cell RNA-seq. *Genome Medicine* 13: 82, doi: 10.1186/s13073-021-00894-y.

Zhou, Y., Luo, K., Liang, L., Chen, M. and He, X. (2023). A new bayesian factor analysis method improves detection of genes and biological processes affected by perturbations in single-cell CRISPR screening. *Nature Methods* 20: 1693–1703, doi: 10.1038/s41592-023-02017-4.

Methods

Given the data matrix Y, consider the decomposition

$$Y = R\,Z + \gamma_{\text{offset}} + \varepsilon \tag{6}$$

with the $G \times P$-dimensional matrix R, the $P \times C$ matrix Z, the $G \times C$ matrix ε, the G-dimensional vector γ_{offset} (all real-valued), and $P < \min(G, C)$. To simplify interpretation, we require the columns of R to be orthonormal (i.e., they are an orthonormal basis of a P-dimensional linear subspace of $\mathbb{R}^G$). The embedding Z can then be considered the P-dimensional coordinates of C points in that linear subspace, each representing a cell. Setting γ_{offset} to the row-wise means of Y, the matrices Z and R are fit by minimizing the sum of squared residuals

$$\sum_{g=1}^{G}\sum_{c=1}^{C} \varepsilon_{gc}^2. \tag{7}$$

Principal component analysis (PCA) is a special case, where in addition the columns of R are obtained from an eigendecomposition and ordered by eigenvalue. In the applications considered in this work, $P \ll \min(G, C)$, and R and Z can be considered a lower-dimensional approximation of the full data matrix $Y - \gamma_{\text{offset}}$.

We extend (6) to incorporate known covariates for each cell. Thus, we consider not just a single matrix R and a single vector γ_{offset}, but treat them as functions of the covariates,

$$\begin{aligned} R &: \mathbb{R}^K \to \{A \in \mathbb{R}^{G\times P} | A^T A = I_P\} \\ \gamma &: \mathbb{R}^K \to \mathbb{R}^G, \end{aligned} \tag{8}$$

where the arguments of these functions are rows of the $C \times K$ design matrix X, i.e., elements of $\mathbb{R}^K$. The output $R(x)$ is an orthonormal $G \times P$ matrix and the output $\gamma(x)$ is a $\mathbb{R}^G$ vector. Model (6) then becomes, for each cell c,

$$Y_{:c} = R(X_{c:})\,Z_{:c} + \gamma(X_{c:}) + \varepsilon_{:c}. \tag{9}$$

Setting $\gamma(X_{c:})$ to the least sum of squares solution of regressing Y on X, the matrix Z and $R \in \mathcal{R}$ are fit by minimizing the sum of squared residuals (7), where $\mathcal{R}$ is a suitable set of matrix-valued functions that we define in the following. Model (9) with these additional features can be considered a multi-condition extension of PCA.

Intuitively, this *multi-condition PCA* finds a function R that generates for each condition (for each distinct row of the design matrix X) a P-dimensional subspace that minimizes the distance to the observed data in that condition by rotating a common *base space* into the optimal orientation (Fig. 1C Step 1). Z is the orthogonal projection of the data on the corresponding subspace. Stability is ensured by constraining R to come from a set $\mathcal{R}$ of "well-behaved", smooth functions of the covariates.

To construct $\mathcal{R}$, we need to recall some concepts from differential geometry. Given the whole numbers G and P, the set of all orthonormal real matrices of dimension $G \times P$ is a differentiable manifold, the Stiefel manifold $V_P(\mathbb{R}^G)$. For our application, it is appropriate to consider two matrices equivalent iff they span the same linear subspace of $\mathbb{R}^G$. The set of all such equivalence classes is again a differentiable manifold, called the Grassmann manifold $\mathrm{Gr}(G, P)$ (Edelman et al., 1998; Bendokat et al., 2023). Accordingly, elements of $\mathrm{Gr}(G, P)$ are P-dimensional linear subspaces of the ambient space $\mathbb{R}^G$. Computationally, we represent an element of $\mathrm{Gr}(G, P)$ by an orthonormal matrix, i.e., by one of the members of the equivalence class.

We then construct $\mathcal{R}$ as the set of all functions R that have domain and codomain as in Eqn. (8) and can be written as

$$R_B(x) = \mathrm{Exp}_o^{(\mathrm{Gr})}\left(\sum_{k=1}^{K} x_k B_{::k}\right), \tag{10}$$

where B is a 3-dimensional real-valued tensor of size $G \times P \times K$. The expression $\mathrm{Exp}^{(\mathrm{Gr})}$ is the exponential map on the Grassmann manifold. It takes a point $o \in \mathrm{Gr}(G, P)$ and a tangent vector at that point, and returns a new point on the Grassmann manifold. Thus, given a choice of the point o, which we call the *base point*, and of the design matrix X, the set of all possible B induces $\mathcal{R}$, and fitting Model (9) is achieved by fitting B. We use the terms *tangent vector* and *tangent space* in their standard meaning in differential geometry and represent tangent vectors with $G \times P$ matrices. The name *exponential map* derives from the fact that for some Riemannian manifolds the exponential map coincides with the matrix exponential; however, this is not the case for Grassmann manifolds. Here the exponential map for a base point o and a tangent vector represented by $A \in \mathbb{R}^{G\times P}$ is

$$\begin{aligned} \mathrm{Exp}_o^{(\mathrm{Gr})}(A) = {} & o\,V\ \mathrm{diag}(\cos d)\,V^T \\ & + U\ \mathrm{diag}(\sin d)\,V^T, \end{aligned} \tag{11}$$

Table 1 | Notation used in the manuscript.

Symbol	Meaning
Y'	Raw count data ($Y' \in \mathbb{Z}_{\geq 0}^{G \times C}$)
Y	Data after size factor normalization and variance-stabilizing transformation ($Y \in \mathbb{R}^{G \times C}$)
$\tilde{Y}$	Data after regressing out the linear effects ($Y - \gamma(X)$)
X	Design matrix ($X \in \mathbb{R}^{C \times K}$)
Z	Position of each cell in the low-dimensional embedding ($Z \in \mathbb{R}^{P \times C}$)
Δ	Predicted differential expression values between two conditions ($\Delta \in \mathbb{R}^{G \times C}$)
P	Number of embedding dimensions. The associated index variable is p.
K	Number of covariates. The index variable is k.
G	Number of genes. The index variable is g.
C	Number of cells. The index variable is c.
$\gamma(x)$	Function that takes a vector of covariates (a row of X) and returns a vector with the offset for each gene ($\gamma(x) \in \mathbb{R}^G$)
Γ	Linear coefficients of $\gamma(x)$ ($\Gamma \in \mathbb{R}^{G \times K}$)
$R(x)$	Function that takes a vector of covariates (a row of X) and returns a matrix with orthonormal columns ($R(x) \in \mathrm{Gr}(G, P)$). Its role is analogous to the principal vectors in PCA.
B	3-tensor of parameters that determines $R(x)$. Each slice $B_{::k}$ represents an element of the tangent space $\mathcal{T}_o \mathrm{Gr}(G, P)$.
o	The base-point ("zero") for the Grassmann exponential map ($o \in \mathrm{Gr}(G, P)$)
$S(x)$	Function that takes a vector of covariates and returns an invertible matrix ($S(x) \in \mathbb{R}^{P \times P}$)
W	3-tensor of parameters for $S(x)$. Each slice $W_{::k} \in \mathbb{R}^{P \times P}$

where $A = U \operatorname{diag}(d) V^T$ is the singular value decomposition of A (Edelman et al., 1998)

The argument of the exponential map in Eqn. (10) is a linear combination of the slices of B. Each slice of $B_{::k}$ represents a tangent vector ($B_{::k} \in \mathcal{T}_o \mathrm{Gr}(G, P)$) and so are their linear combinations (a tangent space is a vector space).

We analogously parameterize the offset function $\gamma(x) = \sum_k \Gamma_{:k} x_k$, where $\Gamma \in \mathbb{R}^{G \times K}$. Accordingly, fitting γ is just ordinary linear regression.

Non-distance preserving extension

Multi-condition PCA (Eqn. (9)) fits subspaces that approximate the data for each condition, but does not depend on shape, scale, or more generally, the statistical distribution of the cells' embeddings in that subspace. Therefore it can also not adjust for ("absorb") such differences. This rigidity increases stability and can be a desirable model feature for some applications, by preventing overfitting, but for other applications it can also be a limitation. We extend Model (9) with an additional, optional term S, a non-distance preserving, affine isomorphism of $\mathbb{R}^P$, to (i) obtain additional flexibility and (ii) enable input of prior knowledge and user preferences in cell matching:

$$Y_{:c} = R(X_{c:}) S(X_{c:}) Z'_{:c} + \gamma'(X_{c:}) + \varepsilon_{:c}. \quad (12)$$

Here, $Z'_{:c} \coloneqq S^{-1}(X_{c:})(Z_{:c} - s_0(X_{:c}))$. The extra term $S(x)$ distinguishes Eqn. (12), the LEMUR model, from its special case for $S \equiv I$, multi-condition PCA, Eqn. (9). To allow translations, we also change $\gamma'(x) = \gamma(x) + R(X_{c:})s_0(x)$, with s_0 defined below.

Next, we describe the selection of S and s_0. It is designed to enable the analyst to state preferences which sets of cells from different conditions should be considered matching each other, i.e., are the same or highly similar. We expect such a specification as a (potentially, and indeed typically, incomplete) partition of the cells $\{1, \ldots, C\}$ into E sets that we call $\mathbb{E}_1, \ldots, \mathbb{E}_E$. This partition is, for example, derived from a set of matching cell type annotations (landmarks) or Harmony's maximum diversity clustering. This provision of preferences is optional; if it is lacking, $E = 0$, the first term in expression (13) vanishes, the optimization simply results in $S = I$, the identity, and LEMUR reverts to multi-condition PCA. S is obtained as a solution to the optimization problem

$$\begin{aligned} \underset{S, s_0 \in \mathcal{S},}{\arg\min} \sum_{e=1}^{E} \sum_{c \in \mathbb{E}_e} \Big(M_e - S^{-1}(X_{c:}) \\ (Z_{:c} - s_0(X_{c:}) \Big)^2 + \lambda(||W^{(0)}||_2^2 + ||W||_2^2) \end{aligned} \tag{13}$$

where the optimization domain $\mathcal{S}$ is described in the next paragraph, and $M_e = |\#\mathbb{E}_e|^{-1} \sum_{c \in \mathbb{E}_e} Z_{:c}$ is the mean latent space coordinate of the cells in similarity set $\mathbb{E}_e$.

The optimization domain $\mathcal{S}$, that is, the set of possible $S(x)$ and s_0, is the set of affine transformations

$$\begin{aligned} S(x) &= I + \sum_{k=1}^{K} x_k W_{::k} \\ s_0(x) &= \sum_{k=1}^{K} x_k W^{(0)}_{:k}, \end{aligned} \tag{14}$$

which is parameterized by the 3-tensor W with dimensions $P \times P \times K$ and the $P \times K$ matrix $W^{(0)}$.

The parameter λ regularizes the optimization and pulls the result towards $S(x) = I$ and $s_0(x) = 0$.

Implementation

We fit multi-condition PCA, Eqn. (9) by:

1. Solving the linear regression for Γ, treating $R(x)$ and Z as 0.
2. Optimizing on the Grassmann manifold for the parameters B of the function R, keeping Γ fixed.
3. Inferring $Z_{:c}$ by projecting $Y_{:c}$ on the orthonormal basis $R(X_{:c})$.

In Step 1, we solve a linear regression for Γ

$$\hat{\Gamma} = \underset{\Gamma}{\arg\min} ||Y - \Gamma X^T||_2^2. \tag{15}$$

In Step 2, we need to solve the manifold regression problem

$$\underset{B_{::k} \in \mathcal{T}_o \mathrm{Gr}(G,P)}{\arg\min} \left| \tilde{Y}_{:c} - \mathrm{Exp}_o \left(\sum_k B_{::k} X_{ck} \right) Z \right|^2, \tag{16}$$

where $\tilde{Y} = Y - \hat{\Gamma} X^T$. We choose the base point o as the first P principal vectors of fitting PCA to full, centered data matrix $\tilde{Y}$.

To optimize B, we build on the work of Kim et al. (2014). They developed an algorithm to approximate the geodesic regression problem

$$\underset{B_{::k} \in \mathcal{T}_o \mathcal{M}}{\arg\min}\ d \left(\Omega_i, \mathrm{Exp}_o \left(\sum_k B_{::k} X_{ik} \right) \right), \tag{17}$$

where $\mathcal{M}$ is a Riemannian manifold, $\Omega_i \in \mathcal{M}$ are data points on the manifolds, and

$$d(p, q) = \sqrt{\langle \mathrm{Log}(p, q), \mathrm{Log}(p, q) \rangle} \tag{18}$$

is the geodesic distance between two points on $\mathcal{M}$. Here, Log is the inverse of the exponential map.

If the observations Ω_i are close to each other, the solution to Eqn. (17) is well approximated by the solution to a standard linear regression in the tangent space

$$\underset{B_{::k} \in \mathcal{T}_o \mathcal{M}}{\arg\min}\ (\mathrm{Log}(o, \Omega_i) - (\textstyle\sum_k B_{::k} X_{ik}))^2 \tag{19}$$

for a base point $o \in \mathcal{M}$ that is close to the center of all Ω_i.

Another step is required before we can apply Kim et al. (2014)'s algorithm, since in our case, the observations $\tilde{Y}_{:c}$ are not elements of the manifold (in our case, $\mathcal{M}$ is the Grassmann manifold $\mathrm{Gr}(G, P)$). We partition $\{1, \ldots, C\}$, the set of all cells, into sets of cells that share the same condition: $\mathbb{D}_1 \cup \ldots \cup \mathbb{D}_D = \{1, \ldots, C\}$ and $\forall d \in 1, \ldots, D : \forall c_1, c_2 \in \mathbb{D}_d : X_{c_1:} = X_{c_2:}$. Then, for each d (i.e., for each group of cells under the same conditions) we find an orthonormal basis

$U_d \in \mathrm{Gr}(G, P)$ using PCA on $\tilde{Y}_{:\mathbb{D}_d}$, the data for these cells only. We then approximate a solution of Eqn. (16) by linear regression weighted by the number of observations per condition ($\#\mathbb{D}_d$) on the U_d projected into the tangent space of o. For this, we plug $\Omega_i = U_d$ into Eqn. (19) with

$$\mathrm{Log}^{(\mathrm{Gr})}(A, B) = U \ \mathrm{diag}(\tan^{-1}(d))\, V^T, \quad (20)$$

where U, V, and d come from an SVD of $(B - AA^TB)(A^TB)^{-1} = U\,\mathrm{diag}(d)V^T$ (Absil et al., 2004).

Non-distance preserving extension

We fit the parameters of W and $W^{(0)}$ using ridge regression after forming the mean M_e for each condition.

Post-processing

After fitting the LEMUR model, we adjust the base space so that the rows of Z are sorted in descending order of their variance, i.e., we take our specific set of basis vectors and adjust them so that they may be interpreted analogously to principal components, as pointing in the direction of highest, second-highest, ... variance. Specifically, we calculate a singular value decomposition of Z

$$Z = U\,\mathrm{diag}(d)V^T. \quad (21)$$

We then set the base point to

$$\tilde{o} = o\,U, \quad (22)$$

adjust the coefficients of R to

$$\tilde{B}_{::k} = B_{::k}\,U \quad (23)$$

and set the low-dimensional embedding Z to

$$\tilde{Z} = \mathrm{diag}(d)V^T. \quad (24)$$

Cluster-free differential expression

The parametric model of the multi-condition single-cell data learned LEMUR can be used for intra- and extrapolation, that is, for prediction. First, for any observed cell, it predicts its gene expression in any of the conditions, even though each cell was only observed exactly once. Second, as each cell is parameterized by a position in latent space, the model can also predict expression of "synthetic cells" at any (unobserved) position z in the latent space for any condition x. We use these capabilities for differential expression analysis. Using the inferred parameters for $\gamma(x)$, $R(x)$, and $S(x)$, we write

$$f(x, z) = R(x)S(x)z + \gamma(x), \quad (25)$$

where f is a function that predicts the gene expression of a cell at latent space position z in the embedding space for any condition x.

Thus, the predicted differential expression for all genes in cell c between conditions 1 and 2 ($d_1, d_2 \in \mathbb{R}^K$) is

$$\Delta_{:c} = f(d_2, Z_{:c}) - f(d_1, Z_{:c}). \quad (26)$$

Differential expression neighborhoods

We use a stochastic sampling algorithm that works on the differential expression matrix Δ to identify *neighborhoods* of cells that show consistent differential expression. Intuitively, these are intended to be sets of cells that cluster together in latent space, i.e., are similar or related cell types and cell states, that also show consistent differential expression with respect to the contrast of interest.

In a first step, we sample many one-dimensional projections of the embedding Z. Specifically, we repeat the following N times: randomly sample two cells from $\{1, \ldots, C\}$, compute the vector between them, $v = Z_{:c_1} - Z_{:c_2}$, and project the data from all cells onto v. This results in the matrix (w_{cn}), where $n = 1, \ldots, N$ indexes the random samples and c indexes the cells. We choose N large enough that there is a good chance that interesting differential expression patterns are apparent in one or more of the $w_{:n}$'s.

Next, for each gene g, we identify the best of these one-dimensional data projections by choosing an n_g for which $w_{:n_g}$ has the maximal absolute correlation to $\Delta_{g:}$. Intuitively, this selects a direction in latent space along which there is differential expression for that gene. We compute the order statistic $(i_1, \ldots, i_C)$ of $w_{:n_g}$, for each $c = 1, \ldots, C$ compute the t-statistic for the sample $\Delta_{g,i_1}, \ldots, \Delta_{g,i_c}$, choose the c_g which maximizes that statistic, and set $\mathbb{Q}_g = \{i_1, \ldots, i_{c_g}\}$.

Pseudobulk differential expression analysis

The pseudobulk approach accounts for the fact that the most relevant unit of replication in multi-condition single-cell data is the sample (and not

the cells) (Crowell et al., 2020). It works by summing the counts across cells within a sample from the same cell subpopulation (e.g., "cell type"). If the data were obtained from F samples, the information which cell belongs to which sample implies a partition of $\{1, \ldots, C\}$ into F sets of cells, which we call $\mathbb{F}_1, \ldots, \mathbb{F}_F$.

Let $Y' \in \mathbb{Z}_{\geq 0}^{G \times C}$ be the count matrix from which Y was constructed. Then we form the pseudobulk count matrix $V \in \mathbb{Z}^{G \times F}$ as

$$V_{gf} = \sum_{c \in \mathbb{F}_f \cap \mathbb{Q}_g} Y'_{gc}, \tag{27}$$

for $f = 1, \ldots, F$, and calculate a gene-specific size factor

$$\mathrm{SF}_{gf} = \sum_{c \in \mathbb{F}_f \cap \mathbb{Q}_g} \sum_{h=1}^{G} Y'_{hc}. \tag{28}$$

This construction differs from the usual pseudobulk approach as it uses a different set of cells $\mathbb{Q}_g$ for each gene.

To address the post-selection inference problem (we want to make inference on the statistical significance of an observed trend based on a test statistic that was itself constructed after consulting the data), we compute (27) on a set of held out cells, which are matched via the (w_{cn}) matrix. The fraction of cells that we assign to the training set (which is used to compute the neighorhoods $\mathbb{Q}_1, \ldots, \mathbb{Q}_G$), and to the test set (which is used to compute the pseudobulk data (27)) balances the power for accurately identifying neighborhoods with interesting gene expression changes, versus the power to provide statistical significance statements for those identifications. Future work may find more elegant solutions.

Relation to other methods

Relation to GSFA

Zhou et al. (2023) described a model for the analysis of perturbation single-cell data called *guided sparse factor analysis* (GSFA) which is related to the SupSVD model (Li et al., 2016). It is build around matrix factorization of the observed data

$$\begin{aligned} Y &\approx RZ \\ Z &\approx \beta X^T. \end{aligned} \tag{29}$$

The model uses sparse priors on R and β to identify which gene modules are related to which latent factors. Unlike LEMUR, model (29) makes the latent embedding Z dependent on the design matrix X.

The sparsity priors favor situations where a perturbation only affects a small number of latent factors in Z and thus columns of R. In that case, the contrast between the subspaces spanned by the active factors of R and the inactive factors for a perturbation has a similar interpretation as the corresponding comparison in LEMUR. However, LEMUR directly identifies the subspaces per condition and does not need to rely on the indirect effect of the sparsity priors.

Relation to GEDI

A recent preprint by Madrigal et al. (2023), published after the first preprint of this work (doi: 10.1101/2023.03.06.531268), presents a model for cluster-free differential expression analysis, similar to what we delineate by Step 1 in Fig. 1A. Their model can be summarized as

$$Y_{:\mathbb{F}_f} = R(X_{f:}) Z_{:\mathbb{F}_f} + \Gamma X_{f:}^T, \tag{30}$$

where $\mathbb{F}_f$ are the indices of all cells from sample f and X is a design matrix on the sample level $(F \times K)$. They define the function R as the linear combination of a reference state (θ_r) and deviations from that reference state (δ)

$$R(x) = \theta_r + \sum_k x_k \delta_k. \tag{31}$$

This model is fairly similar to LEMUR's as it also works by treating the subspace as a function of the covariates. The biggest difference with our model is that their R does not enforce the orthonormality constraints on $R(x)$. The resulting degeneracy between R and Z is partially resolved by scaling each row of Z to a length of 1 and regularization on R, which can optionally be guided by gene-regulatory networks.

Relation to interaction models

Model (9) can express interactions between known covariates and the latent position of each cell. For example, a drug perturbation might affect the gene expression of cells early in a developmental trajectory more than in mature cells. Our model simultaneously identifies the latent position and the interacting drug effect. Yet, the way the interactions are modeled here differs from that in ordinary linear models.

Interactions in ordinary linear models are formed using a direct (Hadamard) product between two or more known covariates. For example, the effectiveness of trastuzumab on breast cancer cells depends on their HER2 status, i.e., the drug is more effective if the HER2 protein level is high. Accordingly, we could model cell viability as a function of

$$\hat{y} = \beta_0 + \beta_1\, x_{\text{conc.}} + \beta_2\, x_{\text{HER2}} + \beta_3\, x_{\text{conc.}} \odot x_{\text{HER2}} \tag{32}$$

and call β_3 the interaction coefficient.

LEMUR's multi-condition PCA model (9) and the interaction model (32) are closely related. To demonstrate, we define R not as eq. (10) but as

$$R(x) = \sum_k B_{::k} x_k, \tag{33}$$

and assume that X contains the known drug concentration from our example above, while Z contains the latent *HER2* status:

$$X = \begin{pmatrix} | & | \\ 1 & x_{\text{conc.}} \\ | & | \end{pmatrix}, \quad Z = \begin{pmatrix} | & | \\ 1 & x_{\text{HER2}} \\ | & | \end{pmatrix}^T. \tag{34}$$

When we plug eqn. (33) into $\hat{Y}_{:c} = R(X_{c:}) Z_{c:}$, we can rewrite it as

$$\hat{Y} = \sum_{p,k} B_{:kp} \left(X_{:k} \odot Z_{p:} \right), \tag{35}$$

which is just a different way to write eq. (32). This demonstrates that the only difference between the interaction model with latent factors and LEMUR is the choice of R.

Interaction model (35) has been used to model the effects of regulatory variants in single-cells across cell states (Cuomo et al., 2022; Nathan et al., 2022). There, the cell states were represented using continuous factors Z; however, the estimation proceeded step-wise: first, estimating Z using PCA or Harmony and only then fitting the interaction coefficients B.

Independent of the parametrization (Eqn. (10) or Eqn. (33)), $R(x)$ can be interpreted as spanning the space that best approximates the observations from condition x. The advantage of Eqn. (10) is that the constraints of the Grassmann manifold naturally map to this intuition. In contrast, the parametrization of Eqn. (33) does not enforce orthonormality between the columns of $R(x)$, it does not even enforce a common scale. This makes the model degenerate when inferring Z and B simultaneously.

Geometrically, the columns of B in Eqn. (33) that correspond to the intercept in X span a base space. All other columns in B are vectors that point out of that base space. In contrast, the $B_{::k} \in \mathcal{T}_o\text{Gr}(G, P)$ in Eqn. (10) correspond to rotations of the base space. For small angles between the spaces of two conditions, there is little difference between a rotation and the straight vector. Thus, one can interpret our multi-condition PCA model as approximating a conventional interaction model between observed and latent covariates.

Execution details

Glioblastoma analysis

We downloaded the count data and patient annotations from GSE148842. We transformed the counts using the function shifted_log_transform from the transformGamPoi package and filtered out all genes with a total of less than 6 counts. We filtered out all cells which did not pass the quality filters from the scuttle package's perCellQCFilters function, and also those cells that had less than 800 or more than 12 000 counts.

We assigned the cell types and tumor status following the methods from the original publication (Zhao et al., 2021). We clustered the Harmony integrated data with walktrap clustering into four clusters. Zhao et al. (2021) identified a chromosome 7 duplication and 10 deletion in all samples. Accordingly, we assigned the cluster which showed upregulation of genes from chromosome 7 and downregulation of genes from chromosome 10 as the tumor cells. The other three clusters were assigned based on marker genes as shown in Fig. 2C.

We ran LEMUR with 60 latent dimensions and a test fraction of 50% and otherwise used the same defaults as in the differential expression benchmark. The full dataset consisted of three conditions: control, panobinostat, and etoposide. For the analysis, we decided to focus on the contrast between panobinostat and control and do not show any data from etoposide-treated cells.

The color scale of Δ in Fig. 2E,F was capped at the 95% quantile of the absolute values and squishing more extreme values to the range. The difference of difference test in the rightmost panel of Fig. 2F was significant at FDR < 0.1 considering all genes with a significant difference (FDR < 0.1) between control and panobinostat inside the neighborhood.

We identified gene ontology terms related with up and down-regulated genes using the clusterProfiler package's enrichGO function on the 200 genes with the smallest p-value comparing them against the universe of genes that passed quality control.

Zebrafish embryonic development analysis

The data downloaded from GSE202639 was already quality-controlled. We subsetted the full dataset to the control cells (*ctrl-inj* and *ctrl-uninj*) for the 16 time points between 18 hours and 48 hours and the 2 000 most variable genes. We transformed the counts using transformGamPoi package's shifted_log_transform function and fit a natural spline model with three degrees of freedom and 80 latent dimensions. We tested the difference between the 48 hour and the 18 hour time point using the settings from the differential expression benchmark.

For the interpolation in Fig. 3B, we sampled cells and linearly interpolated their latent position. We projected ten synthetic cells onto the 2-dimensional UMAP embedding. We calculated the mean of the observed expression values from the 50 nearest neighbors to five synthetic cells at interpolation points 0, 0.25, 0.5, 0.75 and 1. We predicted the gene expression according to LEMUR's spline fit for all ten synthetic cells at 50 time points equally spaced between 18 and 48 hours.

Alzheimer plaque spatial analysis

We downloaded the expression data for the four mouse hippocampi with the Alzheimer plaque densities from the BROAD's single-cell repository. We subsetted the genes to a common set and filtered out lowly expressed genes (total counts per gene less than 50). We further filtered out cell with more than 20% mitochondrial reads and less than 200 or more than 5 000 total counts.

We fit LEMUR with 30 latent dimensions and a test fraction of 60% on an ordered factor of the plaque density cut into ten equally sized bins. We contrasted the largest bin against the smallest bin using the same settings as in the differential expression benchmark.

Integration and prediction benchmark

The integration benchmark measured the ability of methods to adjust for known covariates while retaining the biological structure of the data. The prediction benchmark measured for the tools which support it how well they are able to predict the expression of a cell in arbitrary conditions.

For both benchmarks, we used 13 single-cell datasets (Angelidis et al., 2019; Aztekin et al., 2019; Bhattacherjee et al., 2019; Bunis et al., 2021; Cano-Gamez et al., 2020; Goldfarbmuren et al., 2020; Hrvatin et al., 2018; Jäkel et al., 2019; Kang et al., 2018; Pijuan-Sala et al., 2019; Reyfman et al., 2019; Sathyamurthy et al., 2018; Skinnider et al., 2021) which we downloaded from publicly available sources (see Data Availability for details).

We preprocessed each dataset using transformGamPoi package's shifted_log_transform function with the default parameters. We identified the 500 most variable genes and held out 20% randomly chosen cells.

For the integration benchmark, we compared CPA version 0.8.3 (Lotfollahi et al., 2023), Harmony version 1.1.0 (Korsunsky et al., 2019), LEMUR with $S \equiv I$ (multi-condition PCA), LEMUR with R fixed principal vectors of $\tilde{Y}$ (parametric Harmony), and the full LEMUR model. As a negative control, we used PCA using the fast implementation from the irlba package (version 2.3.5.1).

For the prediction benchmark, we did not consider Harmony, as it does not support going back from the integrated embedding to the gene expression space. Instead, we included two other controls: a linear model-based method that predicts the mean of each condition and another negative control called *identity prediction* that returned the original expression observed for a cell independent of the requested condition.

We tried to run all methods as much as possible with the default parameters. We ran CPA with 64 latent dimensions, 2000 training epochs, and a batch size of 1024. We specified is_count_data = FALSE and recon_loss = 'gauss'.

For LEMUR, we used 30 latent dimensions and a test fraction of 0%. We ran PCA with 30 latent dimensions.

For the evaluation of the integration results displayed in Fig. 4B, we used the integration performance of the held out data compared to the training data except for Harmony which cannot integrate unseen data after the original training step. To make the output of the different methods comparable, we brought each embedding to a common scale by subtracting the mean for each latent dimension and dividing by the average cell vector length. On this rescaled input, we calculated nine different metrics. Four metrics were used to assess the adjustment for the known covariates:

k nearest neighbor (kNN) mixing We identified the $k = 20$ nearest neighbors from the training data for each cell from the held out data. We then calculated how many of those 20 neighbors were from the same condition as the original cell. We averaged these values across all held out cells to derive a single metric for each dataset and method pair.

Maximum mean discrepancy (MMD) We calculated the MMD discrepancy with a radial basis function kernel between the held out and training data after subsampling both to a common number of cells (Gretton et al., 2012). We calculated the discrepancy using scaling factors between 10 and 10^{-3} (50 values, log spaced) and 100, 200, and 500 cells and finally averaged the results to get a single metric.

Wasserstein distance We calculated the Wasserstein distance between held out and training cells using the `wasserstein` function from the `transport` package after subsampling to a common number of cells. We averaged the results for 100, 200, and 500 cells.

Variance explained by condition We calculated the ratio of residual variance after accounting for known covariates over the total variance of the embedding.

We used another four metrics to assess how well each embedding retained the biological information

Adjusted Rand index (ARI) We performed PCA with 30 latent dimensions on one condition of the original log-transformed data and performed walktrap clustering on the result. Then we performed walktrap clustering on the embedding of the held out cells from the same condition fixing the number of clusters to the one obtained in the initial clustering. Then we calculated the adjusted Rand index to measure the cluster consistency using the `ARI` function from the `aricode` package.

Adjusted mutual information (AMI) We followed the same procedure as for the ARI, but calculated the adjusted mutual information using the `AMI` function.

Normalized mutual information (NMI) We followed the same procedure as for the ARI, but calculated the normalized mutual information using the `NMI` function.

Variance explained by cell type We calculated the ratio of residual variance after accounting for the cell types as annotated in the original data over the total variance of the embedding.

Lastly, we also considered one merged metric that directly contrasts the adjustment for the known covariates and the retainance of the biological information

Variance explained by condition vs. cell type We calculated the ratio of residual variance after accounting for the known conditions plus the cell types over the residual variance accounting only for the cell types.

For the prediction benchmark, we considered a total of ten metrics. We considered two conditions for each dataset and always calculated the predicted expression for condition B for cells from condition A against the observed expression in condition B and vice versa.

L_2 mean The L_2 distance between the mean prediction against the mean observed expression across the whole data.

L_2 mean per cell type The L_2 distance between the mean prediction against the mean observed expression for each cell type.

L_2 of the standard deviation (S.D.) The L_2 distance between the standard deviation of the prediction against the standard deviation of the observed expression across the whole data.

L_2 of the S.D. per cell type The L_2 distance between the standard deviation of the prediction against the standard deviation of the observed expression for each cell type.

R^2 mean The correlation between the mean prediction against the mean observed expression across the whole data.

R^2 mean per cell type The correlation between the mean prediction against the mean observed expression for each cell type.

R^2 of the S.D. The correlation between the standard deviation of the prediction against the standard deviation of the observed expression across the whole data.

R^2 of the S.D. per cell type The correlation between the standard deviation of the prediction against the standard deviation of the observed expression for each cell type.

Maximum mean discrepancy (MMD) We calculated the MMD discrepancy between the predicted and observed data after subsampling to a common number of cells with a radial basis function kernel (Gretton et al., 2012). We calculated the discrepancy using scaling factors between 10 and 10^{-3} (50 values, log spaced) and 100, 200, and 500 cells and finally averaged the results to get a single metric.

Wasserstein distance We calculated the Wasserstein distance between predicted and observed data using the `wasserstein` function from the `transport` package after subsampling to a common number of cells. We averaged the results for 100, 200, and 500 cells.

Variance explained comparison

For all 13 datasets used in the integration and prediction benchmark, we compared the fraction of variance explained by LEMUR and by PCA. To make the results comparable, we manually regressed out the effects of the known covariates. We compared irlba's approximate PCA implementation and the LEMUR model accounting for the known covariates. We fixed the `linear_coefficient_estimator ="zero"` as we had already manually removed the linear effects. We measured the elapsed time using R's `system.time` function.

Differential expression and neighborhood inference benchmark

For the differential expression benchmark, we took the gene expression values of the top 8000 highly variable genes from individual conditions and appended 200 simulated genes. We assigned each cell to a synthetic control or treatment condition. This ensured that for all original genes there was no real differential expression, whereas for the 200 simulated genes we were able to control the number of cells with a differential expression pattern and the log fold change.

We only considered the dataset-condition combinations which had the most independent replicates. We chose two conditions from the Angelidis et al. (2019); Goldfarbmuren et al. (2020); Kang et al. (2018) data, three conditions from Hrvatin et al. (2018) and one from Sathyamurthy et al. (2018). Thus, we had eleven datasets in total.

We then simulated 200 genes for each dataset with varying number of affected cells. We first performed k means clustering on the 50-dimensional embedding of the data with either 2, 3, 10, or 20 clusters. Then for each gene we chose one of the clusters and fixed the log fold change to 0.5, 1, 2, or 4 respectively (i.e., for the smaller clusters, we used a larger effect size). The counts were simulated according to

$$\begin{aligned} Y_{gc} &= \text{GammaPoisson}(\mu = 2^{\eta_{gc}}\text{sf}_c, \alpha = 0.2) \\ \eta_{gc} &= \beta_g^{(0)} + \beta_g^{(\text{DE})} x_c^{(\text{is DE})} + \beta_g^{(\text{samp } 1)} x_c^{(\text{samp } 1)} + \cdots \end{aligned} \tag{36}$$

where $\beta_g^{(\text{DE})}$ is the log fold change, $x_c^{(\text{is DE})}$ indicates if cell c is inside the selected cluster, and $\beta_g^{(\text{samp } 1)} x_c^{(\text{samp } 1)}$ simulates a sample-specific effect where $\beta_g^{(\text{samp } i)}$ is drawn from a normal distribution a standard deviation of 0.1.

Using the known set of simulated genes (true positive) and original genes (true negatives), we calculate the true positive rate (TPR, fraction of identified true positives) and false discovery rate (FDR, fraction of false positives among all positives).

Our default settings for LEMUR in the differential expression benchmark were

- 30 latent dimensions,
- a test fraction of 50%,
- `directions ="randomized"`,

- selection_procedure ="zscore",
- size_factor_method ="normed_sum",
- and test_method="edgeR".

In addition, we tested several variations:

- LEMUR with test_method set to *glmGamPoi* (Ahlmann-Eltze and Huber, 2020) or *limma* (Smyth, 2004),
- LEMUR with 8 or 80 latent dimensions,
- LEMUR with a test fraction of 20% and 80%,
- LEMUR with size_factor_method ="ratio",
- LEMUR with directions ="contrast" or selection_procedure ="contrast",
- LEMUR with $S \equiv I$ (skip alignment) or R fixed to the principal vectors of $\tilde{Y}$ (parametric Harmony),
- LEMUR where we reused the training data for testing,
- LEMUR where the test and training data were generated through count splitting (Neufeld et al., 2022).

We compared the FDR and TPR from LEMUR against seven alternative methods:

Global test A single test with *edgeR* or *glmGamPoi* across the full dataset.

Cell type test One test per cell type (using the annotation from the original data) with *edgeR* or *glmGamPoi*.

Cluster test One test per walktrap cluster on the Harmony integrated data with *edgeR* or *glmGamPoi*.

MiloDE One test per Milo neighborhood using *edgeR* (Missarova et al., 2023).

For the *cell type test*, *cluster test*, and MiloDE, which perform more than one test per gene, we considered a group of cells as positive if they contained more than 60% changed cells (at least 10). If none of the cell groups for a gene fulfilled this criterion, the group with the largest fraction of changed cells was considered as positive. A group of cells was considered negative if less than 10% of the cells were changed. If the fraction of changed cells was between 10% and 60% the status for that group of cells was considered indeterminate and the group was ignored for the TPR and FDR calculation.

Supplementary Figures

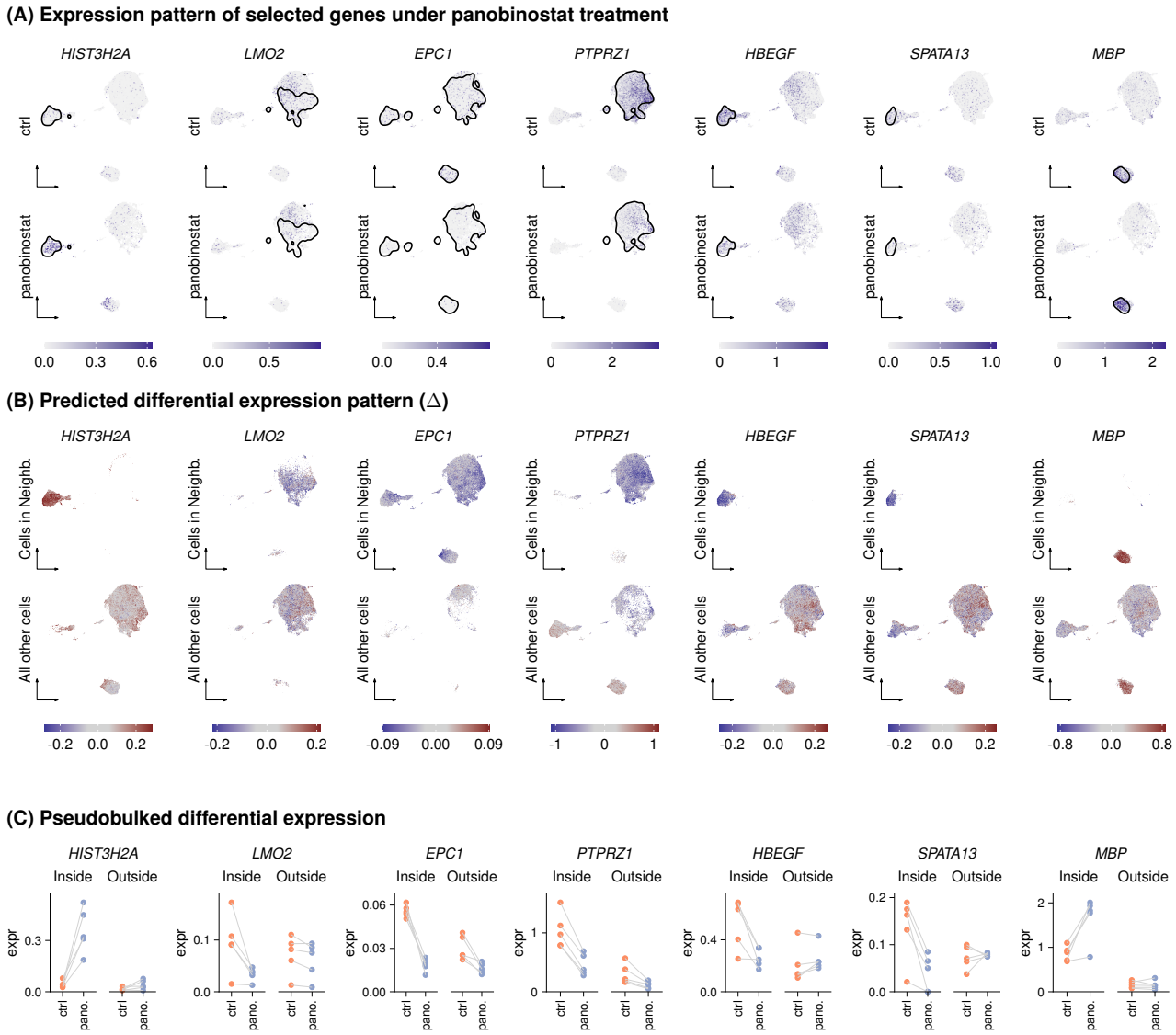

Suppl. Figure S1: Differential expression patterns for seven genes with the neighborhoods inferred by LEMUR. (A) UMAPs colored by gene expression (log-normalized counts). The black line encircles 80% of the cells inside the gene-specific differential expression neighborhood. (B) UMAPs colored by predicted expression change per cell. The cells are separated depending if they are inside or outside the neighborhood. (C) Scatter plot of the pseudobulked expression values per condition, neighborhood status and sample.

(A) Zebrafish: tissue labels plus zoom in on cell types in central nervous system and periderm

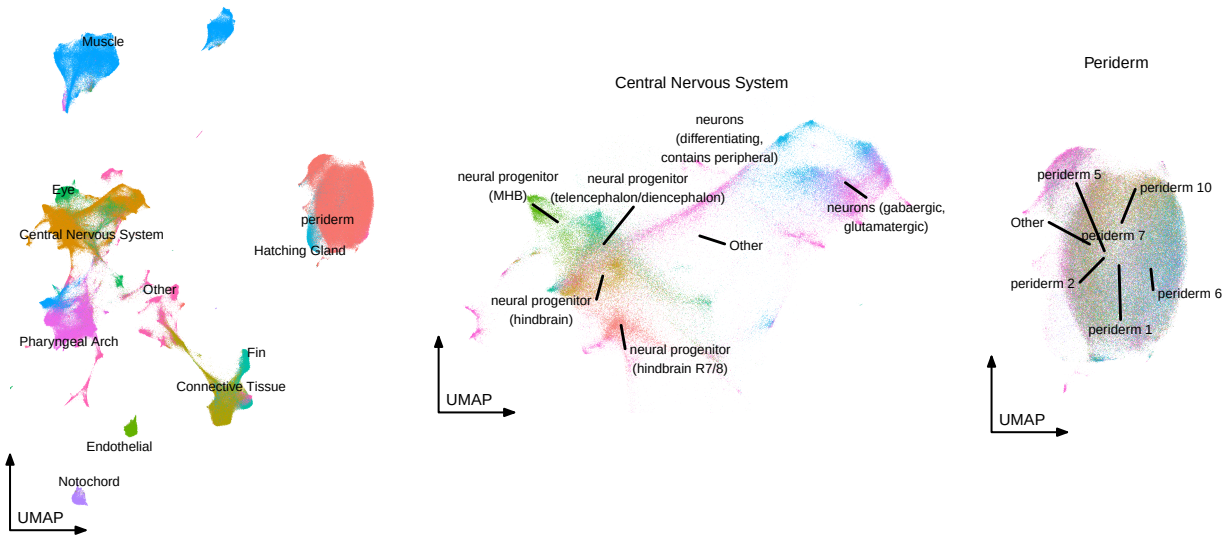

(B) Mouse hypocampus: broad cell type labels

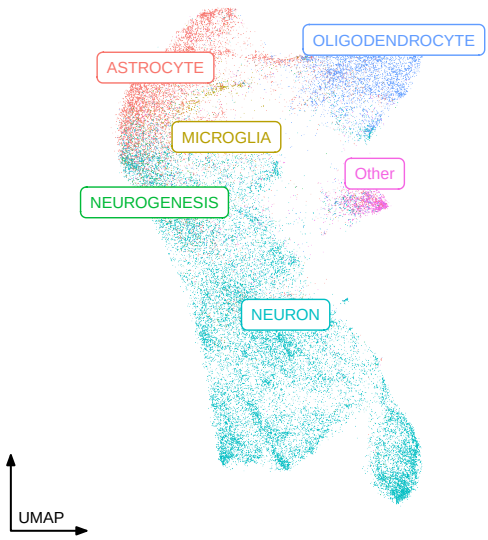

Suppl. Figure S2: Cell type annotation for zebrafish and mouse brain datasets. (A) Left panel: UMAP of the full timecourse data with cells colored by tissue type as annotated in Saunders et al. (2023). Middle and right panel: Cell type annotations for central nervous system and periderm also from Saunders et al. (2023). (B) Cell type annotation for the cells from the four mouse hippocampi annotated using the data from Saunders et al. (2018) as reference.

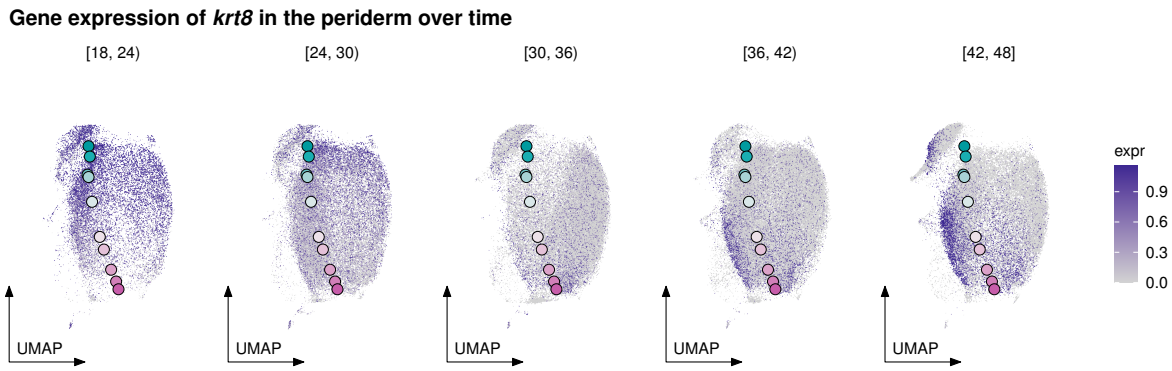

Suppl. Figure S3: Gene expression of *krt8* in the periderm over time. The overlayed points are the synthetic cells from Fig. 3B.

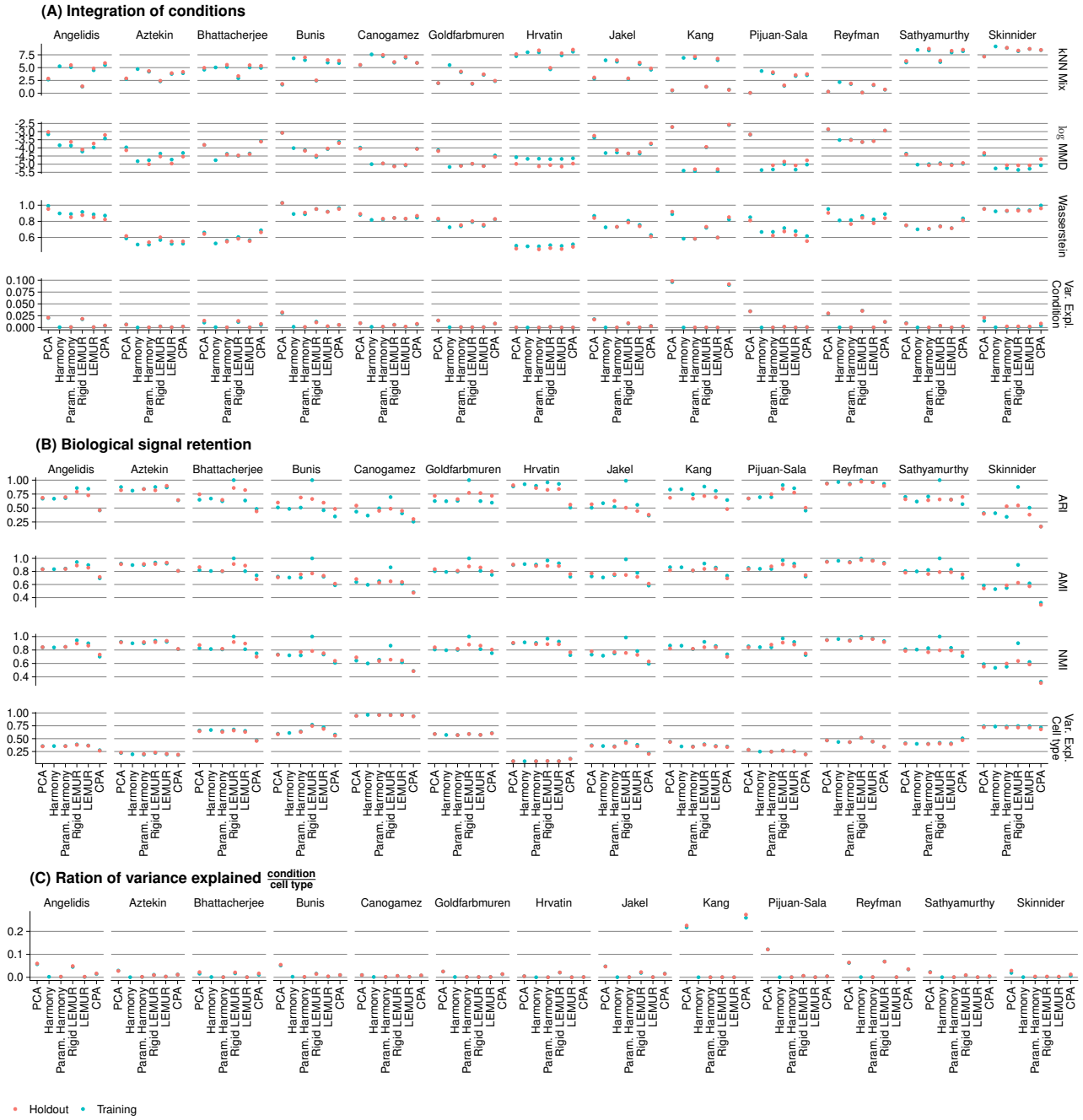

Suppl. Figure S4: Comparison of integration performance across 13 datasets. (A) A scatter plot of four metrics that measure how well each method adjusted for the known covariates. Higher values indicate better performance for k-NN mixing and worse performance for the other metrics. (B) A scatter plot of four metrics that measure how well each method retained the biological signal. Higher values indicate better performance for all metrics. (C) A scatter plot of an integrated performance measure comparing the ratio of variance explained by the known covariates vs cell types (as a proxy for the biological signal). Higher values indicate worse performance. The red points show the performance for data not seen during training (holdout) and in blue for the data seen during training.
k-NN: k nearest neighbors, MMD: maximum mean discrepancy, var. expl.: variance explained, ARI: adjusted Rand index, AMI: adjusted mutual information, NMI: normalized mutual information, rigid LEMUR: LEMUR with $S = I$.

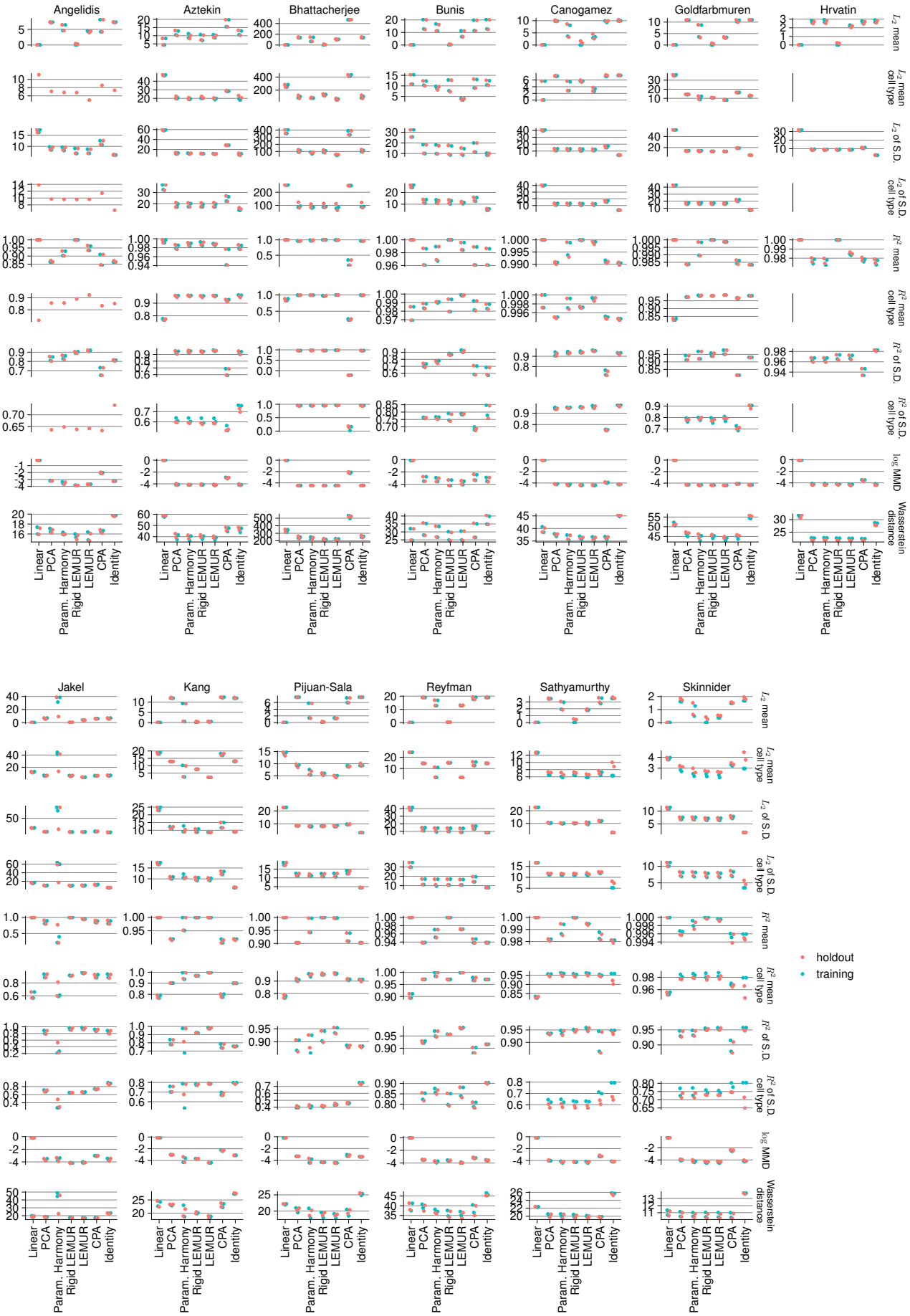

Suppl. Figure S5: *See next page.*

Suppl. Figure S5: Comparison of the prediction performance across 13 datasets for the two metrics show in Fig 4E and eight additional metrics. For each metric, we show the values for cells from the control condition against treated condition and for cells from the treated condition again control condition. The red points show the performance for data not seen during training (holdout) and in blue for the data seen during training. L_2 measures the distance between the mean of the prediction against the mean of the observed expression values. Lower values are better. Similarly, the R^2 measures the correlation between predicted and observed values. Here, higher values are better. Both metrics are calculated either for the overall mean, the mean per cell type, the overall standard deviation or the standard deviation per cell type. The log of the maximum mean discrepancy (MMD) and the Wasserstein distance are both non-parametric measures how similar the prediction and observed values are. Lower values are better.
S.D.: standard deviation, MMD: maximum mean discrepancy, , rigid LEMUR: LEMUR with $S = I$.

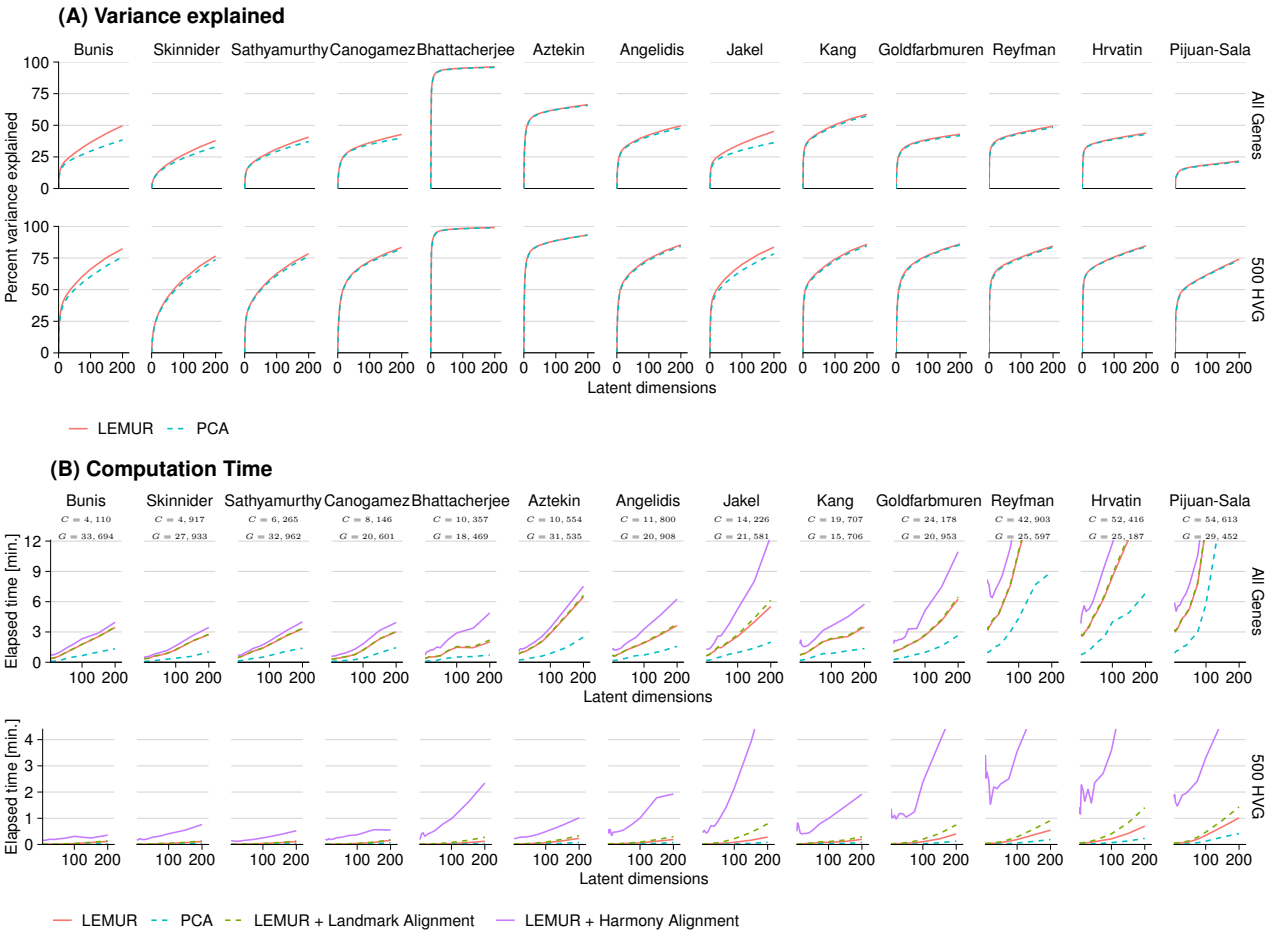

Suppl. Figure S6: (A) Line plot of number of latent dimensions against the variance explained for PCA and LEMUR. (B) Line plot of number of latent dimensions against the computation time for PCA, LEMUR, and LEMUR with landmark or Harmony-based alignment.

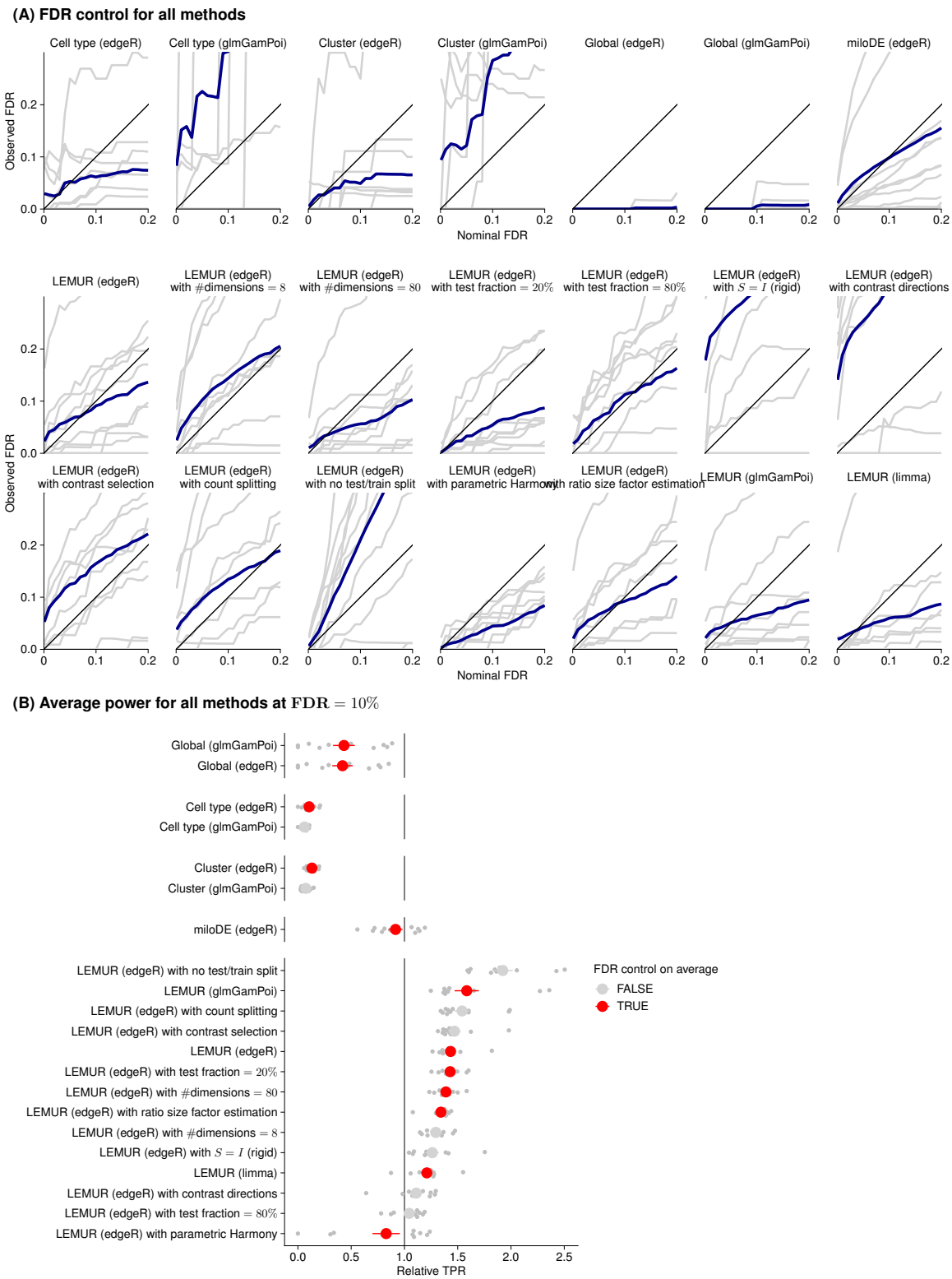

Suppl. Figure S7: FDR control and power for all methods across eleven datasets. (A) Line plot of the nominal FDR against the observed FDR. The blue line shows the average. (B) Scatter plot of the relative TPR at an FDR = 10% for each method across eleven datasets normalized by the mean per dataset. The point range shows the mean and standard error. If the average observed FDR is larger than 10% the point is greyed out.
FDR: false discovery rate, TPR: true discovery rate

Suppl. Table S1: Overview of the patients from whom the glioblastoma biopsies originated.

Patient ID	Age	Gender	Tumor location	Conditon	# Cells
PW030	65	M	right parietal	vehicle (DMSO)	17384
				0.2 uM panobinostat	5686
PW032	61	M	left frontal	vehicle (DMSO)	5003
				0.2 uM panobinostat	738
PW034	68	F	left parieto-occipital	vehicle (DMSO)	12375
				0.2 uM panobinostat	1761
PW036	56	M	right temporal	vehicle (DMSO)	10292
				0.2 uM panobinostat	2558
PW040	69	M	right temporal	vehicle (DMSO)	8901
				0.2 uM panobinostat	1257